INTERFEROMETRY OF ε AURIGAE: CHARACTERIZATION OF THE ASYMMETRIC ECLIPSING DISK

B. K. Kloppenborg[1,2,9], R. E. Stencel[2], J. D. Monnier[3], G. H. Schaefer[1], F. Baron[1], C. Tycner[4], R. T. Zavala[5], D. Hutter[5],
M. Zhao[6], X. Che[3], T. A. ten Brummelaar[1], C. D. Farrington[1], R. Parks[1], H. A. McAlister[1], J. Sturmann[1], L. Sturmann[1],
P. J. Sallave-Goldfinger[1], N. Turner[1], E. Pedretti[7], AND N. Thureau[8]

[1] The CHARA Array of Georgia State University, Mount Wilson Observatory, Mount Wilson, California 91023, USA; bkloppenborg@chara.gsu.edu
[2] Department of Physics & Astronomy, University of Denver, Denver, CO 80208 USA
[3] Department of Astronomy, University of Michigan, 941 Dennison Building, Ann Arbor, Michigan 48109, USA
[4] Department of Physics, Central Michigan University, Dow Science Complex 219, Mount Pleasant, Michigan, 48859, USA
[5] United States Naval Observatory, Flagstaff Station, 10391 West Naval Observatory Road, Flagstaff, Arizona 86001, USA
[6] Department of Physics and Astronomy, Penn. State, University Park, PA 16802
[7] School of Engineering and Physical Sciences, Heriot Watt University, Edinburgh, Scotland, UK
[8] University of St. Andrews, Scotland, UK

ABSTRACT

We report on a total of 106 nights of optical interferometric observations of the ε Aurigae system taken during the last 14 years by four beam combiners at three different interferometric facilities. This long sequence of data provides an ideal assessment of the system prior to, during, and after the recent 2009 2011 eclipse. We have reconstructed model-independent images from the 10 in-eclipse epochs which show that a disk-like object is indeed responsible for the eclipse. Using new three-dimensional, time-dependent modeling software, we derive the properties of the F-star (diameter, limb darkening), determine previously unknown orbital elements (Ω, i), and access the global structures of the optically thick portion of the eclipsing disk using both geometric models and approximations of astrophysically relevant density distributions. These models may be useful in future hydrodynamical modeling of the system. Finally, we address several outstanding research questions including mid-eclipse brightening, possible shrinking of the F-type primary, and any warps or sub-features within the disk.

Key words: binaries: eclipsing   techniques: interferometric   techniques: photometric

Supporting material: figure sets

1. INTRODUCTION

Epsilon (ε) Aurigae (FKV 0183, HD 31964) is an intrinsically bright ($V \sim 3.0$) star system that has confounded generations of astronomers since its two-year long, $\Delta V \sim 0.75$ mag fading was first discovered nearly 200 years ago (Fritsch 1824). In the early 1900s, it was established that ε Aurigae was a single-line spectroscopic binary with a 27.1 year period (Ludendorff 1903). Application of the then recently developed eclipsing binary theory (Russell 1912a, 1912b) to ε Aurigae came to the perplexing result: the companion must be nearly equal in mass to the primary, but nearly invisible (see note 18 of Shapley 1915). Although many theories have been proposed to explain this conundrum (see Carroll et al. 1991; Guinan et al. 2002; Kloppenborg 2012, for comprehensive summaries of the literature), it was Kopal (1954) who first proposed and Huang (1965) who later (independently) developed the theory that the system is a nearly edge-on eclipsing binary composed of an F0Ia supergiant (primary, hereafter the F-star) and an unseen companion that was believed to be enshrouded in a disk of opaque material. It was theorized that the passage of the disk in front of the F-star caused the anomalously long fading of the system. This theory received significant support during the 1984 eclipse when Backman et al. (1984) detected the presence of a 500 ± 150 K blackbody that remained detectable when the F-star was eclipsed.

The 2009 2011 eclipse of ε Aurigae caused a resurgence of interest in this enigmatic binary, yielding a wealth of new scientific results. Historic data played a pivotal role in several studies. Stefanik et al. (2010) and Chadima et al. (2010) published two new, nearly identical, spectroscopic orbital solutions using spectroscopic and photometric data going back to the mid-1800s. Likewise, Griffin & Stencel (2013) conducted a meticulous study of historic and new spectroscopic observations covering the three eclipses. They discovered that the precision by which the spectroscopic evolution of the eclipse unfolds indicates that the structure of the disk has not appreciably changed on a time scale of at least the last 100 years. Similarly, infrared studies reported by Stencel et al. (2011) have confirmed persistent behavior of disk features over at least the last two eclipse cycles.

New photometric and spectroscopic observations have revealed the progression of the eclipse in hitherto unprecedented detail. Photometric monitoring, largely by amateur astronomers, captured nearly 3700 photometric points in a myriad of filters from the UV to near-IR (Hopkins 2012). Spectroscopic monitoring has shown that the equivalent width of some spectral lines follow a stair step-like evolution pattern (Leadbeater et al. 2012), suggesting some substructure exists within the eclipsing disk. For the first time, a comprehensive spectral energy distribution (SED) of the system was assembled from the UV to radio wavelengths. These data clearly show the presence of not only the F-star and a 550 K disk, but also a slight amount of far-UV flux thought to originate from a B-type companion at the center of the disk (Hoard et al. 2010). Subsequent work has shown the disk has an asymmetric temperature structure ranging from 550 1150 K due to external heating from the F-star (Hoard et al. 2012).

---

[9] Max Planck Institut Für Radioastronomie.

		Form Approved OMB No. 0704-0188

Report Documentation Page

1. REPORT DATE **SEP 2015**	2. REPORT TYPE	3. DATES COVERED **00-00-2015 to 00-00-2015**

4. TITLE AND SUBTITLE **Interferometry of E Aurigae: Characterization of the Asymmetric Eclipsing Disk**	5a. CONTRACT NUMBER
	5b. GRANT NUMBER
	5c. PROGRAM ELEMENT NUMBER
6. AUTHOR(S)	5d. PROJECT NUMBER
	5e. TASK NUMBER
	5f. WORK UNIT NUMBER

7. PERFORMING ORGANIZATION NAME(S) AND ADDRESS(ES) **United States Naval Observatory, Flagstaff Station,,10391 West Naval Observatory Road,,Flagstaff,,AZ,86001**	8. PERFORMING ORGANIZATION REPORT NUMBER

9. SPONSORING/MONITORING AGENCY NAME(S) AND ADDRESS(ES)	10. SPONSOR/MONITOR'S ACRONYM(S)
	11. SPONSOR/MONITOR'S REPORT NUMBER(S)

12. DISTRIBUTION/AVAILABILITY STATEMENT **Approved for public release; distribution unlimited**

14. ABSTRACT
We report on a total of 106 nights of optical interferometric observations of the ?? Aurigae system taken during the last 14 years by four beam combiners at three different interferometric facilities. This long sequence of data provides an ideal assessment of the system prior to, during, and after the recent 2009???2011 eclipse. We have reconstructed model-independent images from the 10 in-eclipse epochs which show that a disk-like object is indeed responsible for the eclipse. Using new three-dimensional, time-dependent modeling software, we derive the properties of the F-star (diameter, limb darkening), determine previously unknown orbital elements (??, i), and access the global structures of the optically thick portion of the eclipsing disk using both geometric models and approximations of astrophysically relevant density distributions. These models may be useful in future hydrodynamical modeling of the system. Finally, we address several outstanding research questions including mideclipse brightening, possible shrinking of the F-type primary, and any warps or sub-features within the disk.

15. SUBJECT TERMS

16. SECURITY CLASSIFICATION OF:			17. LIMITATION OF ABSTRACT	18. NUMBER OF PAGES	19a. NAME OF RESPONSIBLE PERSON
a REPORT **unclassified**	b ABSTRACT **unclassified**	c THIS PAGE **unclassified**	**Same as Report (SAR)**	**23**	

In addition to the classic observational methods, the comparatively new technique of optical interferometry was recently applied to the ϵ Aurigae eclipse for the first time. The model-independent H-band images prove, beyond any reasonable doubt, that an eclipsing disk is indeed responsible for the observed fadings (Kloppenborg et al. 2010). Complementary spectro-interferometric observations of the Hα line have shown that the F-star has an extensive P-Cygni-like wind region and that the disk contains a substantial gaseous atmosphere that can eclipse a greater fraction of the F-star than the dark disk itself (Mourard et al. 2012).

Yet with as much information we have about this system, we have yet to unravel many of its fundamental properties. Foremost, the distance to the system is extremely uncertain, ranging from 0.4 4.0 kpc as estimated by *HIPPARCOS* (Perryman & ESA 1997; van Leeuwen 2007). Dynamical parallaxes from the Yerkes (Strand 1959) and Sproul (van de Kamp 1978; Heintz & Cantor 1994) observatories narrow this range to 0.5 0.7 kpc, yet there is in significant disagreement with the 1.5 ± 0.5 kpc suggested via interstellar absorption and reddening (Guinan et al. 2012). Second, the evolutionary state of the system has been called into doubt. Some suggest that the F-star is a massive ($\sim$16 $M_\odot$) horizontal branch supergiant, whereas others consider the F-star to be a less massive ($\sim$2 3 $M_\odot$) post-AGB star (see Guinan et al. 2002; Hoard et al. 2010; Sadakane et al. 2010, for a review and recent developments concerning this topic). Finally, although several models have been proposed for the eclipsing disk (e.g., Huang 1965, 1974; Wilson 1971; Takeuti 1986, 2011; Ferluga 1990; Lissauer et al. 1996; Budaj 2011), these efforts were primarily based on light curve modeling. Reproducing the photometry is a necessary condition of every model, but is not sufficient for proving the validity of the hypothesis. In particular, such work cannot separate out the degeneracies between radial and height-dependent optical profiles in the disk.

We begin to address several of these issues by presenting newly determined orbital elements and new models for the disk based upon simultaneous photometric and interferometric modeling of the 2009 2011 eclipse during the ingress (RJD = JD − 2,400,000 $\sim$ 55,062 55,193), totality (RJD $\sim$ 55,193 55,631), and egress (RJD $\sim$ 55,631 55,693) phases. In Section 2, we present our observations and data reduction methods. Sections 3 and 4 include a discussion of our modeling process, image reconstruction methods, and statistical analysis of the resulting data. Results are presented in Section 5, and finally, we draw conclusions in Section 6.

2. OBSERVATIONS AND DATA REDUCTION

This work summarizes a total of 106 nights of interferometric observations taken by four beam combiners at three different interferometric arrays. An account of the observations including the array, baselines, combiner, spectral configuration, and calibrators is provided in Table 1. Calibrator identifiers, positions, proper motions, uniform disk diameters (θ_{UDD}), and the array at which each calibrator was used are listed in Table 2. The supplementary material for this paper contain both calibrated and uncalibrated data saved in the Optical Interferometry Exchange format (OIFITS; Pauls et al. 2005). A sample plot of the UV coverage, squared visibilities, and bispectra for the 2009-11 CHARA-MIRC epoch is provided in Figure 1. Equivalent plots for all other epochs can be found in the supplementary

material, Figures A1 A45. In the next several paragraphs we describe the interferometric arrays, combiners, and reduction methods in detail.

2.1. Palomar Testbed Interferometer (PTI)

Our first interferometric data set on ϵ Aurigae was acquired using the PTI (Colavita et al. 1999) located on Mount Palomar in California. The facility consisted of three 40 cm siderostats, each located at the termination of one of the interferometer's three arms. Pairwise combination provided baselines between 85 and 110 m. The beam combiner at PTI operated in several low-resolution spectral modes providing up to 11 spectral channels across the K band (2.2 μm).

Much of the wide-band visibility data has been discussed previously in Stencel et al. (2008), therefore, we will not consider it further. Here we have re-reduced the spectrally dispersed (i.e., narrow-band) data subject to the calibrator diameters in Table 2. We have used the narrow- and wide-band calibration routines *nbCalib* and *wbCalib*, respectively, from the *V2calib* software package. These programs are available as a web service, *webCalib*, on the NASA Exoplanet Science Institute (formerly Michelson Science Center) website.[10] We have selected the PTI defaults with the following exceptions: (1) the calibration window was extended to four hours; (2) no ratio correction was applied, and (3) no minimum uncertainty was enforced for reasons discussed in Stencel et al. (2008). Output from this pipeline were saved in OIFITS format.

2.2. Navy Precision Optical Interferometer (NPOI)

The NPOI (Armstrong et al. 1998) is a six telescope optical interferometer that started operation in 1994. The array may be configured in either an astrometric or imaging mode. Data from the imaging subarray comes from six movable 50 cm siderostats with baselines between 16 and 79 m. The NPOI beam combiner operates at visible wavelengths (0.5 0.85 μm) in 16 spectral channels. The NPOI observational setup and data recording procedure can be found in Hummel et al. (2003) and Benson et al. (2003). Post-processing and data reduction were performed using C. Hummel's OYSTER software package.

The NPOI observed ϵ Aurigae on a total of 29 nights between 2006 February and 2010 April as shown in Table 1. The data were initially calibrated with respect to HD 32630 assuming a uniform disk diameter of 0.507 $\pm$ 0.025 milliarcseconds (mas) and saved as OIFITS files. Prior to modeling these data, we recalibrated the OIFITS files by multiplying the visibilities and closure amplitudes by the ratio of the uniform disk function of the former and new diameter as listed in Table 2.

2.3. Center for High Angular Resolution Astronomy (CHARA)

Georgia State University's CHARA (ten Brummelaar et al. 2005) is an interferometric array located on Mount Wilson, CA. The array consists of six 1-m telescopes that can be combined to form up to 15 baselines ranging in length from 34 to 331 m. Using the longest baselines, a resolution of down to 0.5 mas in the H band (0.7 mas in the K band) can be realized.

---

[10] http://nexsciweb.ipac.caltech.edu/cgi bin/webCalib/webCalib.cgi

Table 1
List of Observations from the MIRC, NPOI, CLIMB, and PTI Beam Combiners

Date	JD	Configuration	Array	Combiner/Mode	Calibrators (HD)	Comment
1997 10 22	2,450,744.02	N S	PTI	K band, 7 channels	32630, 33167	
1997 11 09	2,450,761.95	N S	PTI	K band, 11 channels	32630	
1998 11 07	2,451,124.95	N S	PTI	K band, 5 channels	32630	
1998 11 25	2,451,142.94	N S	PTI	K band, 5 channels	30823	
1998 11 26	2,451,143.93	N S	PTI	K band, 5 channels	42807	
2005 12 11	2,453,715.78	N W	PTI	K band, 9 channels	29645	
2006 01 31			PTI	K band	no calibrators	
2006 02 25	2,453,791.74	E06 AC0 AW0, AC0 AE0 AN0	NPOI	16 channels	32630	
2006 02 26	2,453,792.75	E06 AC0 AW0, AC0 AE0 AN0	NPOI	16 channels	32630	
2006 03 03	2,453,432.68	E06 AC0 AW0, AC0 AE0 AN0	NPOI	16 channels	32630	Noisy data on longest baseline
2007 03 02	2,454,161.63	W07 AC0 AN0, AW0 AC0 W07	NPOI	16 channels	32630	
2007 03 05	2,454,164.67	E06 AN0 AW0, E06 AW0 W07	NPOI	16 channels	32630	
2007 03 10	2,454,169.65	E06 AN0 AW0, E06 AW0 W07	NPOI	16 channels	32630	
2007 03 12	2,454,898.63		NPOI	16 channels	32630	Calibrator scans incoherent, unusable
2007 03 13	2,454,172.63	E06 AN0 AW0, E06 AW0 W07	NPOI	16 channels	32630	
2007 03 14	2,454,173.63	E06 AN0 AW0, E06 AW0 W07	NPOI	16 channels	32630	
2007 03 15	2,454,174.63	E06 AN0 AW0, E06 AW0 W07	NPOI	16 channels	32630	
2007 03 16	2,454,175.64	E06 AN0 AW0, E06 AW0 W07	NPOI	16 channels	32630	
2007 10 19	2,454,392.99	N S	PTI	K band, 5 channels	29645	
2007 10 20	2,454,393.97	N S	PTI	K band, 9 channels	30138, 32630	Incoherent v2
2007 10 21	2,454,394.98	N S	PTI	K band, 5 channels	30138	
2007 11 27	2,454,431.85	N S	PTI	K band, 5 channels	27946, 30138, 32537	
2007 12 23	2,454,457.78	N W	PTI	K band, 5 channels	30138, 32630, 33167	Incoherent v2
2007 12 24	2,454,458.75	N W	PTI	K band, 5 channels	32630	
2008 02 16	2,454,512.63	N W	PTI	K band, 5 channels	30138, 32630	
2008 02 17	2,454,513.64	N W	PTI	K band, 5 channels	30138, 32630	
2008 02 18	2,454,514.65	N W	PTI	K band, 5 channels	30138, 32630	
2008 09 19	2,454,729.02	S1 E1 W1 W2	CHARA	MIRC, 4T, LR H, choppers	3360, 22928, 219080	
2008 10 17	2,454,757.00	N W	PTI	K band, 5 channels	32630	
2008 10 26	2,454,765.98	N S, N W	PTI	K band, 5 channels	29645, 30138, 30823, 32630	Incoherent v2
2008 11 07	2,454,777.89	S1 E1 W1 W2	CHARA	MIRC, 4T, LR H, choppers	5448, 101501, 24398, 50019	
2008 11 08	2,454,778.88	S1 E1 W1 W2	CHARA	MIRC, 4T, LR H, choppers	5448, 101501, 24398, 50019	
2008 11 08	2,454,778.87	N S	PTI	K band, 5 channels	29645, 30138, 30823, 32630	
2008 11 09	2,454,779.87	N W	PTI	K band, 5 channels	29645, 30138, 30823, 32630	
2008 11 15	2,454,786.87	N S	PTI	K band, 5 channels	42807, 73262	

Table 1
(Continued)

Date	JD	Configuration	Array	Combiner/Mode	Calibrators (HD)	Comment
						Closest calibrator, HD 32406, is a bad calibrator. Had to use these cals which are >3 hr away.
2008 11 22	2,454,792.82	N S, N W	PTI	K band, 5 channels	30823, 32630	
2008 12 10	2,454,810.82	S1 E1 W1 W2	CHARA	MIRC, 4T, LR H, choppers	101501, 24398	
2008 12 20			PTI		32630	No calibrators in spectral records. Will not calibrate.
2008 12 21			PTI		32630	Only one record, will not calibrate.
2009 03 08	2,454,898.63	E06 AN0 AW0, E06 AW0 W07	NPOI	16 channels	32630	Poor weather
2009 03 12	2,454,902.63	E06 AN0 AW0, E06 AW0 W07	NPOI	16 channels	32630	Poor weather, not used.
2009 11 02	2,455,137.80	S1 E1 W1 W2	CHARA	MIRC, 4T, LR H	32630	
2009 11 02	2,455,137.95	S2 E2 W1 W2	CHARA	MIRC, 4T, LR H	32630	
2009 11 03	2,455,138.79	S1 E1 W1 W2	CHARA	MIRC, 4T, LR H	3360, 24760, 32630	MIRC + PAVO
2009 11 03	2,455,138.98	S2 E2 W1 W2	CHARA	MIRC, 4T, LR H	24760, 32630	MIRC + PAVO
2009 11 04	2,455,139.75	S1 E1 W1 W2	CHARA	MIRC, 4T, LR H	3360, 24760, 32630	
2009 11 04	2,455,139.93	S2 E2 W1 W2	CHARA	MIRC, 4T, LR H	24760, 32630	
2009 12 02	2,455,167.77	S1 E1 W1 W2	CHARA	MIRC, 4T, LR H	32630	
2009 12 02	2,455,167.89	S2 E2 W1 W2	CHARA	MIRC, 4T, LR H	24760, 32630	
2009 12 03	2,455,168.74	S1 E1 W1 W2	CHARA	MIRC, 4T, LR H	24760	
2009 12 03	2,455,168.93	S2 E2 W1 W2	CHARA	MIRC, 4T, LR H	32630, 41636	
2009 12 04	2,455,169.88	S2 E2 W1 W2	CHARA	MIRC, 4T, LR H	24760, 32630, 41636	
2009 12 18	2,455,183.77	AW0 AC0, AE0 AC0	NPOI	16 channels	32630	
2009 12 19	2,455,184.73	AW0 AC0, AE0 AC0	NPOI	16 channels	32630	
2009 12 20	2,455,185.80	AW0 AC0, AE0 AC0	NPOI	16 channels	32630	
2009 12 21	2,455,186.81	AC0 E06 AW0, AE0 AC0 AN0	NPOI	16 channels	32630	
2009 12 25	2,455,190.71	AW0 AC0, AE0 AC0	NPOI	16 channels	32630	Very noisy, little data, not used.
2009 12 27	2,455,192.69	AW0 AC0, AE0 AC0	NPOI	16 channels	32630	
2010 01 03	2,455,199.67	AC0 E06 AW0, AE0 AC0 AN0	NPOI	16 channels	32630	
2010 01 04	2,455,289.60		NPOI	16 channels	32630	All incoherent scans, unusable
2010 01 05	2,455,201.68	AC0 E06 AW0, AE0 AC0 AN0	NPOI	16 channels	32630	
2010 01 06	2,455,202.79	AE0 AN0 AW0, AW0 AE0 AN0	NPOI	16 channels	32630	
2010 01 07	2,455,203.78	AE0 AN0 AW0, AW0 AE0 AN0	NPOI	16 channels	32630	
2010 01 08	2,455,204.66	AE0 AN0 AW0, AW0 AE0 AN0	NPOI	16 channels	32630	
2010 01 09	2,455,205.86	AE0 AN0 AW0, AW0 AE0 AN0	NPOI	16 channels	32630	
2010 01 10	2,455,206.83	AE0 AN0 AW0, AW0 AE0 AN0	NPOI	16 channels	32630	
2010 01 12	2,455,208.77	AE0 AN0 AW0, AW0 AE0 AN0	NPOI	16 channels	32630	Erradic behavior on long baselines, possibly real signal.
2010 01 13	2,455,209.70	AE0 AN0 AW0, AW0 AE0 AN0	NPOI	16 channels	32630	

Table 1
(Continued)

Date	JD	Configuration	Array	Combiner/Mode	Calibrators (HD)	Comment
2010 01 16	2,455,212.69	AC0 E06 AW0, AE0 AC0 AN0	NPOI	16 channels	32630	
2010 02 14	2,455,241.62	AC0 E06 AW0, AE0 AC0 AN0	NPOI	16 channels	32630	
2010 02 15	2,455,242.62	AC0 E06 AW0, AE0 AC0 AN0	NPOI	16 channels	32630	
2010 02 16	2,455,243.62	AC0 E06 AW0, AE0 AC0 AN0	NPOI	16 channels	32630	
2010 02 17	2,455,244.62	AC0 E06 AW0, AE0 AC0 AN0	NPOI	16 channels	32630	
2010 02 18	2,455,245.74	S2 E2 W1 W2	CHARA	MIRC, 4T, LR H	32630, 41636	
2010 02 19	2,455,246.70	S1 E1 W1 W2	CHARA	MIRC, 4T, LR H	No calibrators, used closure phase only	See Text
2010 04 03	2,455,289.60	AN0 E06 AW0, AW0 E06 W07	NPOI	16 channels	32630	
2010 08 20	2,455,428.96	S1 E1 W1 W2	CHARA	MIRC, 4T, LR H	3360, 21770, 24760, 32630	
2010 08 21	2,455,429.96	S2 E2 W1 W2	CHARA	MIRC, 4T, LR H	3360, 21770, 24760, 32630	
2010 08 22	2,455,430.99	S1 E1 W1 W2	CHARA	MIRC, 4T, LR H	21770, 32630	
2010 08 23	2,455,431.96	S2 E2 W1 W2	CHARA	MIRC, 4T, LR H	3360, 21770, 24760, 32630, 219080	
2010 09 23	2,455,462.92	S1 E2 W1 W2	CHARA	MIRC, 4T, LR H	24760, 32630	
2010 09 24	2,455,463.92	S2 E2 W1 W2	CHARA	MIRC, 4T, LR H	3360, 6961, 21770, 219080, 24760, 32630	
2010 09 26	2,455,465.98	W1 W2 S2 E2	CHARA	MIRC, 4T, LR H	32630	MIRC + PAVO
2010 09 27	2,455,466.99	W1 W2 S2 E2	CHARA	MIRC, 4T, LR H	32630	MIRC + PAVO
2010 09 28	2,455,467.97	W1 W2 E2 S2	CHARA	MIRC, 4T, LR H	32630	MIRC + PAVO
2010 10 26	2,455,495.85	S1 E1 W1 W2	CHARA	MIRC, 4T, LR H	24760, 32630	
2010 10 26	2,455,495.98	S2 E2 W1 W2	CHARA	MIRC, 4T, LR H	32630	
2010 10 27	2,455,496.86	S1 E1 W1 W2	CHARA	MIRC, 4T, LR H	32630	
2010 10 27	2,455,496.91	S2 E2 W1 W2	CHARA	MIRC, 4T, LR H	32630	
2010 11 04	2,455,504.95	S2 E2 W1 W2	CHARA	MIRC, 4T, LR H	32630	
2010 11 05	2,455,505.89	S1 E1 W1 W2	CHARA	MIRC, 4T, LR H	21770, 32630, 41636	
2010 12 12	2,455,542.77	W1 W2 E2 S1	CHARA	MIRC, 4T, LR H	32630, 50019	MIRC + PAVO
2010 12 13	2,455,543.75	W1 W2 E2 S1	CHARA	MIRC, 4T, LR H	24760, 32630	MIRC + PAVO
2010 12 14	2,455,544.75	W1 W2 S2 E1	CHARA	MIRC, 4T, LR H	32630	MIRC + PAVO
2011 01 18	2,455,579.67	S1 E1 W1 W2	CHARA	MIRC, 4T, LR H	32630	
2011 01 18	2,455,579.89	S2 E2 W1 W2	CHARA	MIRC, 4T, LR H	32630, 50019	
2011 01 19	2,455,580.66	S1 E1 W1 W2	CHARA	MIRC, 4T, LR H	32630	
2011 01 19	2,455,580.78	S2 E2 W1 W2	CHARA	MIRC, 4T, LR H	32630, 41636	
2011 03 18		E1 E2 W1	CHARA	CLIMB, H	32630	Non standard readout mode and bad conditions. Not usable.
2011 04 01	2,455,652.68	E1 E2 W1	CHARA	CLIMB, K	32630	
2011 04 03	2,455,654.67	S2 W2 W1	CHARA	CLIMB, K	32630	
2011 04 05	2,455,656.66	S2 E1 W1	CHARA	CLIMB, K	32630	
2011 09 18	2,455,823.03	W1 S2 S1 E1 E2 W2	CHARA	MIRC, 6T, LR H	27396	
2011 09 24	2,455,829.03	W1 S2 S1 E1 E2 W2	CHARA	MIRC, 6T, LR H	32630	See Text
2011 10 10	2,455,844.94	W1 S2 S1 E1 E2 W2	CHARA	MIRC, 6T, LR H	32630	
2011 11 03	2,455,868.85	W1 S2 S1 E1 E2 W2	CHARA	MIRC, 6T, LR H	21770, 24760, 32630	

Note. Calibrator IDs may be cross referenced with Table 2.

Table 2
Calibrators and Adopted Uniform Disk Diameters (θ_{UDD})

HD	Name	Position (J2000)		μ_α (mas yr^{-1})	μ_δ (mas yr^{-1})	π (mas)	Published diameters			Adopted		Array	References	Notes
		R.A. (HH MM SS.SS)	decl. (DD MM SS.SS)				θ_{UDD-H} (mas)	θ_{UDD-K} (mas)	$\sigma_{\theta_{UDD}}$ (mas)	θ_{UDD} (mas)	$\sigma_{\theta_{UDD}}$ (mas)			
3360	zet Cas	00 36 58.28419	+53 53 48.8673	17.38	9.86	5.5	0.287	0.288	0.02	0.287	0.020	C	(2)	
5448	37 And	00 56 45.21211	+38 29 57.6380	153.48	36.49	25.14	0.593	0.594	0.042	0.593	0.042	C	(2)	
6961	tet Cas	01 11 06.16225	+55 08 59.6472	226.77	18.75	24.42	…	…	…	0.471	0.033	C	(4)	
21770	36 Per	03 32 26.26028	+46 03 24.6965	52.11	75.26	27.53	…	…	…	0.582	0.041	C	(4)	
22928	del Per	03 42 55.50426	+47 47 15.1746	25.58	43.06	6.32	…	…	…	0.549	0.038	C	(4)	
24398	zet Per	03 54 07.92248	+31 53 01.0812	5.77	9.92	4.34	…	…	…	0.700	0.030	C	(1)	
27396	53 Per	04 21 33.16557	+46 29 55.9554	20.06	35.45	6.43	…	…	…	0.285	0.020	C	(2)	
27946	67 Tau	04 25 25.01518	+22 11 59.9876	111.97	47.71	22.03	0.442	0.443	0.031	0.443	0.031	P	(2)	
28052	71 Tau	04 26 20.74092	+15 37 05.7652	114.31	32.19	20.37	…	…	…	0.542	0.038	P	(4)	
29645	HR 1489	04 41 50.25660	+38 16 48.6622	241.65	97.15	31.38	0.521	0.522	0.037	0.523	0.037	P	(2)	
30138	HR 1514	04 46 44.47871	+40 18 45.3270	9.07	36.83	7.53	0.856	0.86	0.061	0.826	0.061	P	(4)	
30823	HR 1550	04 52 47.75706	+42 35 11.8569	10.63	0.46	7.2	0.317	0.317	0.022	0.317	0.022	P	(2)	Get cal estimates ~0.1 mas larger
32537	9 Aur	05 06 40.62967	+51 35 51.8025	30.49	172.89	38.04	…	…	…	0.589	0.041	P	(4)	
32630	eta Aur	05 06 30.89337	+41 14 04.1127	31.45	67.87	13.4	…	…	…	0.453	0.012	C,P,N	(3)	
33167	HR 1668	05 10 42.92081	+46 57 43.4550	58.34	149.99	20.54	…	…	…	0.498	0.035	P	(4)	
37147	122 Tau	05 37 03.73543	+17 02 25.1776	42.24	33.69	20.58	…	…	…	0.375	0.026	P	(4)	
41636	HR 2153	06 08 23.13611	+41 03 20.6194	1.36	48.55	7.82	…	…	…	0.765	0.054	C	(4)	
42807	HR 2208	06 13 12.50242	+10 37 37.7095	77.38	298	55.71	0.473	0.475	0.034	0.475	0.034	P	(2)	
50019	tet Gem	06 52 47.33887	+33 57 40.5175	1.66	47.31	17.25	0.802	0.804	0.056	0.802	0.056	C	(2)	
73262	del Hya	08 37 39.36627	+05 42 13.6057	70.19	7.9	20.34	0.464	0.465	0.032	0.465	0.032	P	(2)	
101501	61 UMa	11 41 03.01636	+34 12 05.8843	12.55	380.75	104.04	…	…	…	0.864	0.061	C	(4)	
219080	7 And	23 12 33.00380	+49 24 22.3455	90.23	95.56	40.67	…	…	…	0.665	0.047	C	(4)	

Notes. C: CHARA, N: NPOI, P: PTI.
References (1) MIRC Calibrator database, (2) Lafrasse et al. (2010), (3) Maestro et al. (2013), (4) Value computed using SearchCal.

Initial calibration observations of ϵ Aurigae were taken far in advance of the eclipse, in 2008 October/November/December. Semi-regular observations were scheduled around the photometric eclipse, beginning in 2009 October/November and ending in 2011 November. In total, ϵ Aurigae was observed on 38 nights, yielding 19 individual epochs after consecutive nights were merged. The first two eclipse ingress epochs were previously discussed in Kloppenborg et al. (2010) in which reconstructed images and a preliminary model (comprised of an infinitely thin, but optically thick disk seen in projection) for the eclipsing disk were presented.

2.3.1. Michigan InfraRed Combiner (MIRC)

MIRC (described in Monnier et al. 2004; Monnier 2006) went through several revisions during our observing program. As it was first used, the combiner was configured for four-telescope beam combination using a camera sensitive in the H and K bands with three spectral resolution options ($R \sim 44$, 150, or 400). We followed the standard observing procedures and reduced the data using the data reduction pipeline described in Monnier et al. (2007). After co-adding frames, background subtraction, and a Fourier transform of the raw data, fringe amplitudes and phases are used to form the squared visibilities and triple products. These data are written to OIFITS files for further analysis.

In the earliest data, photometric calibration was achieved using choppers that temporally encoded the flux coming from each telescope by periodically blocking each beam at a unique frequency. In 2009 August, the choppers were replaced by dedicated photometric channels (Che et al. 2010) that utilize a fraction of light from each science beam for calibrated, spectrally dispersed photometry. This led to a dramatic improvement in uncertainties. In the spring of 2011, MIRC was upgraded again to combine light from all six of CHARA's telescopes (see initial report in Monnier et al. 2010), permitting measurement of 15 non-redundant visibilities and all 10 independent closure phases available at CHARA.

2.3.2. CLassic Interferometry with Multiple Baselines (CLIMB)

During the egress phase of the 2009 2011 eclipse, when MIRC was unavailable for use, we employed the CLIMB (Sturmann et al. 2010) combiner. CLIMB is a three-telescope beam combiner which operates in one of five broadband spectral modes. For our observations we configured CLIMB in with the K band ($\bar{\lambda} = 2.133 \, \mu$m, FWHM 0.349 μm) filter installed and destructive readout mode. Because of the large hour angle during our observations, the UV coverage afforded by these data is quite limited.

We used the standard observing technique and reduced our data with the CLIMB version 2.1 reduction pipeline (ten Brummelaar et al. 2012). Data were calibrated subject to the calibrators listed in Table 2 and written to OIFITS format for further analysis.

3. MODELING AND ANALYSIS

When our interferometric observations at CHARA began, no publicly available software was capable of modeling both interferometric and photometric data in a fully 3D, time dependent fashion. We wrote two software packages to solve this problem: The SImulation and Modeling Tool for Optical Interferometry (SIMTOI) and the OpenCL Interferometry

Library (liboi). Because there are no prior publications discussing these software, we present a brief overview of their capabilities here.

SIMTOI[11] (Kloppenborg & Baron 2012b) is an open source (GPL) C/C++ program for fitting time-dependent, 3D models to large data sets. Instead of using analytic models, SIMTOI uses the Open Graphics Library (OpenGL) to tessellate the "surfaces" of the astronomical objects being simulated. Geometrical effects, such as limb darkening, are applied using programs written in the OpenGL Shading Language (GLSL). The models may be positioned statically in their 3D environment using fixed Cartesian coordinates or be determined dynamically from a Keplerian orbit. All models also have an intrinsic inclination, i, position angle, Ω, and rotational zero point, ω. The geometrical primitives are rotated, translated, and orthographically rendered to a multisample anti-aliasing buffer. OpenGL computes the total flux in each pixel using a method akin to ray tracing, creating 2D images against which observed data is compared. At present, SIMTOI supports both interferometric and photometric data. Additional data types can be supported by subclassing and registering the new data type with SIMTOI's plugin API. SIMTOI provides a similar API for registering minimization engines. Presently implemented minimizers include a recursive grid search, Levmar (Lourakis 2005), MultiNest (Feroz & Hobson 2008; Feroz et al. 2009), and a bootstrapping minimizer based on Levmar. The validity of models produced by SIMTOI has been tested against iota Peg, the CHARA-MIRC closure phase calibrator (Monnier et al. 2007) and LitPro (Tallon-Bosc et al. 2008) model results.

SIMTOI uses liboi[12] (Kloppenborg & Baron 2012a) to generate interferometric observables. liboi is an open-source (LGPL) C/C++ library which implements the backend from the GPu Accelerated Image Reconstruction (Baron & Kloppenborg 2010) program. liboi aims to provide software developers with convenient access to fast routines for common interferometric tasks. The software heavily relies on the heterogeneous computing environment of the Open Compute Language (OpenCL) to target a wide range of traditional and multi-core CPUs; servers, hand-held/embedded devices, specialized hardware, and Graphical Processing Units (GPUs). The computational correctness of liboi is provided by a series of built-in unit tests to analytical functions.

3.1. Bayesian Model Selection

In this work, we use Bayesian statistics to assess the relative goodness of fit between our proposed models rather than traditional chi-squared methods that are ill-adapted to make such inferences (Marshall et al. 2006). Bayesian statistics provides a consistent approach to estimate a set of parameters, Θ, in a hypothesis (e.g., an image or model), H, given some observed data, D. Bayes' theorem states that

$$P(\Theta|D, H) = \frac{P(D|\Theta, H)P(\Theta|H)}{P(D|H)}, \qquad (1)$$

where $P(\Theta|D, H) \equiv P(\Theta)$ is the posterior probability distribution of the parameters, $P(D|\Theta, H) \equiv L(\Theta)$ is the likelihood, $P(\Theta|H) = \pi(\Theta)$ is the prior, and $P(D|H) \equiv Z$ is the Bayesian Evidence. In parameter estimation problems,

---

[11] SIMTOI: https://github.com/bkloppenborg/simtoi

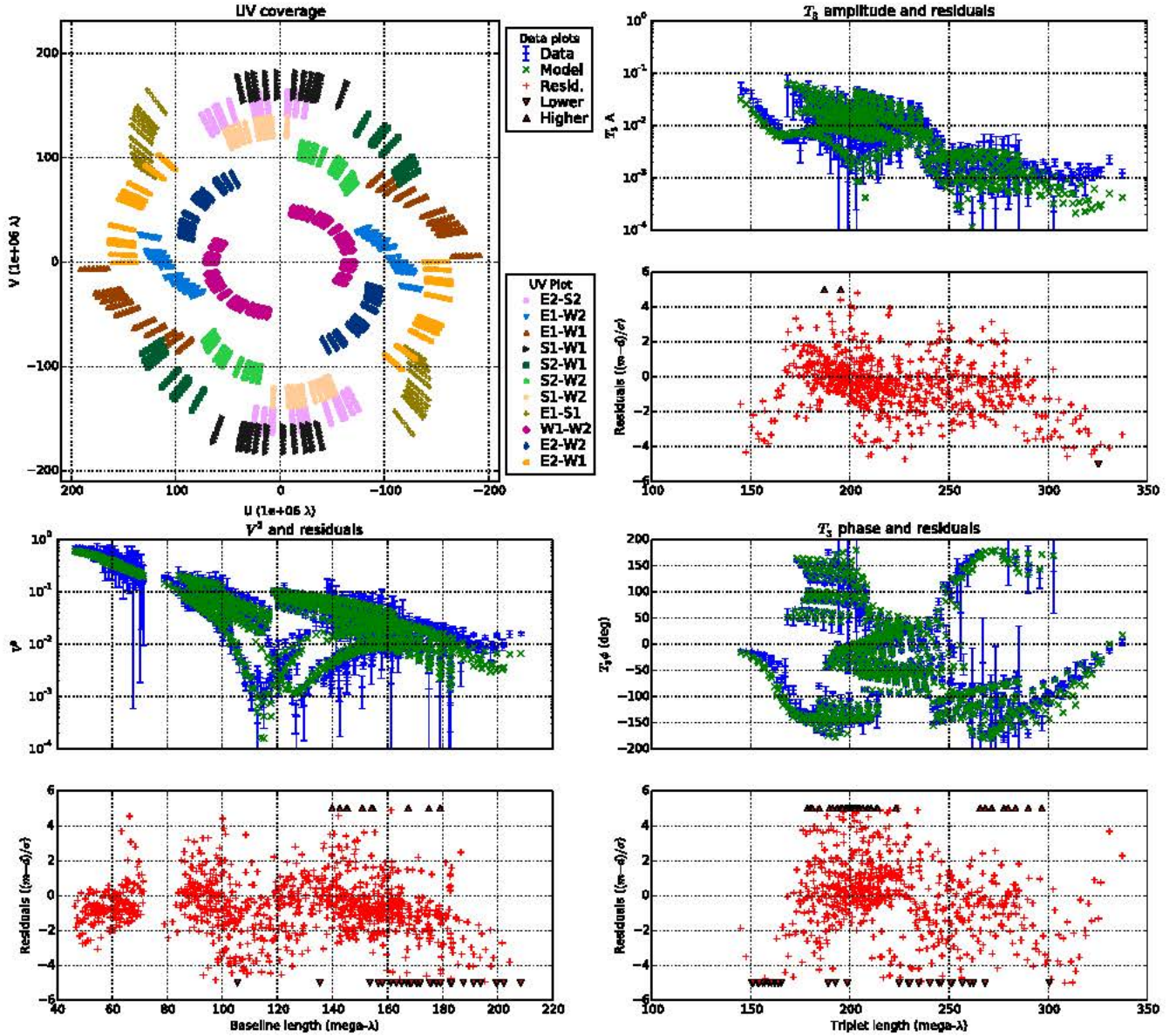[12] liboi: https://github.com/bkloppenborg/liboi

Figure 1. UV coverage, data, best fit bootstrapped model, and residual plot for the 2009 11 CHARA MIRC epoch. These data, taken during the ingress phase of the eclipse, show a clear departure from circular symmetry in all measured quantities as evidenced by the visibilities, triple amplitudes, and closure phases being significantly different at similar baseline/triplet lengths (baseline lengths summed in quadrature). Equivalent figures for other epochs can be found in extended Figures A1 A45.

(The complete figure set (45 images) is available.)

where the model remains the same, the normalization factor, Z, is often ignored as it is independent of the parameters Θ. When selecting between various models, the evidence plays a central role through the Bayes Factor:

$$R = \frac{P\left(H_1|D\right)}{P\left(H_0|D\right)} = \frac{P\left(D|H_1\right)P\left(H_1\right)}{P\left(D|H_0\right)P\left(H_0\right)} = \frac{Z_1}{Z_0}\frac{P\left(H_1\right)}{P\left(H_0\right)}. \quad (2)$$

The evidence is the average of the likelihood over the prior. Thus a simple model with greater likelihood over the parameter range will be favored over a more complex model with lower likelihood over the parameter range, unless the latter is significantly better at explaining the data. Therefore the Bayes factor automatically implements the Occam razor principle.

A principal difficulty in using Bayesian evidence for model selection is that the multidimensional integral,

$$P(D|H) \equiv Z = \int L(\Theta)\pi(\Theta)d^D\Theta, \quad (3)$$

must be evaluated. For this work, we decided to use the *MultiNest* library (Feroz & Hobson 2008; Feroz et al. 2009, 2013) that numerically estimates this integral by intelligently exploring the parameter range using Markov chain methods and ellipsoidal bounding conditions. In the model fitting process we have assumed non-informative (flat) priors and used the standard likelihood function:

$$L(\Theta) = \prod_i \frac{1}{\sqrt{2\pi\sigma_i^2}} \exp\left[\frac{\left(M(\Theta)_i - D_i\right)^2}{2\sigma_i^2}\right], \quad (4)$$

where $M(\theta)_i$ is the model prediction, D_i is the data, and σ_i is the uncertainty associated for the ith data point.

3.2. F-star Model

Within the *SIMTOI* framework, the F-star is modeled as a single uniformly illuminated sphere, located at the origin, to which GLSL shaders (simulating limb darkening) were applied. The PTI observations are very high up on the visibility curve, therefore, they provide no reliable measurement of limb darkening. Consequently, we fit all PTI data with a uniform disk model. The CHARA and NPOI observations frequently resolve the F-star near or beyond the first visibility null. These data show clear departures from uniform disk behavior. To account for this, we implemented several limb darkening laws in GLSL. These include linear, logarithmic, square root, power law (via. Hestroffer 1997), and a few multi-parameter laws (e.g., Claret 2000; Claret & Hauschildt 2003; Fields et al. 2003).

3.3. Disk Models

The previous models for the ϵ Aurigae disk were purely geometric representations with hard edges (e.g., Kloppenborg et al. 2010; Kloppenborg 2012, and references therein). In this work, we have created geometric and astrophysical density distribution models with position-dependent optical properties. Because of the edge-on nature of the eclipse, we elected to represent all disks as a series of concentric rings of infinitesimal thickness and uniform total height, h, that are equally spaced between an inner, r_{in}, and outer, r_{out}, radius. The rings are connected at the midplane by another surface.

Inspired by the appearance of proplyds in the Orion Nebula (e.g., Ricci et al. 2008), the geometrical models have opacity (via. OpenGL source transparency, src_{α}) that is controlled by a double power law that is a function of radius and height:

$$src_{\alpha}(r, z) = \left(\frac{r}{r_{out}}\right)^{-\alpha}\left(\frac{z}{h/2}\right)^{-\beta}. \quad (5)$$

For the two astrophysical disk models, we keep the concentric ring representation of the disk, but modify the opacity of each ring according to a real density distribution. The first model from Pascucci et al. (2004) consists of a power law in the radial direction and a scale height exponential taper in the vertical direction:

$$\rho(r, z) = \rho_0\left(\frac{r}{r_c}\right)^{-\alpha}e^{-\frac{1}{2}\left(\frac{z}{h}\right)^2}, \quad (6)$$

where ρ_0 is the density, r_c is the scale radius, $h = h_c\left(\frac{r}{r_c}\right)^{-\beta}$, h_c is the scale height, and units are in angular quantities (e.g., mas or mas ^{3} when appropriate). The second density distribution is characterized by a power-law in the inner disk and an exponential taper at large radii (cf. Andrews et al. 2009):

$$\rho(r, z) = \rho_0\left(\frac{r}{r_c}\right)^{-\gamma}e^{-\frac{1}{2}\left(\frac{z}{h}\right)^2}e^{-\left(\frac{r}{r_c}\right)^{2-\gamma}}. \quad (7)$$

For these models, the OpenGL transparency is calculated as $src_{\alpha} = 1 - e^{-\kappa(\lambda)\rho(r,z)}$ to ensure the pixel intensity is computed following radiative transfer conventions. Because the composition and precise optical properties of the disk have yet

to be ascertained, we have treated the product $\kappa_0\rho_0$ as a single quantity in our minimization.

In this work we also introduce time-dependence by positioning the disk according to a Keplerian orbit. The spectroscopic orbital solutions from Stefanik et al. (2010) and Chadima et al. (2010) are in excellent agreement with each other; however, the astrometric orbital parameters are not well constrained. Therefore, our model adopts the spectroscopic orbital parameters (longitude of periastron, ω, eccentricity, e, period, P, and time of periastron, T) from Stefanik et al. (2010) and we derive the astrometric parameters (inclination, i, longitude of the ascending node, Ω, and total orbital semimajor axis, α_T) via. minimization to our data.

3.4. Modeling Process

Within the framework of the aforementioned models, the number of parameters needed ranges from 6 in the case of a uniformly illuminated F-star and cylindrical disk (e.g., i, Ω, α_T, θ_{UDD}, r_{disk}, and h_{disk}) to 10 with a limb darkened disk and more complex opacity model for the disk (see Table 4 for a summary of all parameters used and their permitted ranges). To reduce the number of degrees of freedom, we elected to establish bounds by solving a series of subproblems first, then lift restrictions to generalize the results.

1. First, use Bayesian evidence and the post-eclipse CHARA-MIRC data to establish bounds for the diameter and limb-darkening of the F-star.
2. Once determined, the diameter was used to approximate the total orbital semimajor axis, α_T, for the system using two methods. To first order, we may assume the orbit is circular and the eclipse transects the equator of the F-star. Then α_T may be found, to first order, by equating the fraction of the orbit spent in ingress, with the equivalent sector of the orbit via,

$$\frac{T}{t_{ingress}} = \frac{p}{s} \approx \frac{2\pi\alpha_T}{\theta_{star}}, \quad (8)$$

where p is the perimeter of the orbit, s is the orbital sector, α_T is the separation of the components, and θ_{star} is the diameter of the F-star in radians. If $s \ll p$, we may perform a second-order approximation for the sector using the Ramanujan approximation for the perimeter of an ellipse. In this case, we find:

$$\frac{T}{t_{ingress}} \approx \pi\alpha_T\left[3\left(1 + \sqrt{1 - e^2}\right) - \sqrt{10\sqrt{1 - e^2} + 3(2 - e^2)}\right]\frac{\cos\omega}{\theta_{star}}, \quad (9)$$

where ω and e are the aforementioned orbital quantities.

3. Approximate the position angle of the ascending node, Ω, by computing the average of the position angles determined from single-epoch in-eclipse minimizations.
4. Determine the best-fit disk model by performing a simultaneous fit to the photometric and interferometric data. The F-star's diameter and limb darkening are held constant. α_T and i are free, whereas Ω, ω, e, P, and T are constant.
5. Derive the best-fit F-star's diameter, limb darkening coefficient, disk height, and disk transparency at each epoch while holding the remaining parameters constant.

6. Finally, lift the constraints on our models insofar as possible to derive statistical information of the aforementioned parameters via bootstrapping individual epochs.

4. IMAGE RECONSTRUCTION

We performed image reconstruction for the figures presented in this publication using both SQUEEZE (Baron et al. 2010), a logical successor to the Markov Chain Imager (MACIM Ireland 2006), and the BiSpectrum Maximum Entropy Method (BSMEM; Buscher 1994; Baron & Young 2008). The theory behind image reconstruction, namely the minimization of the χ^2 datum plus a regularization function, is common to these packages; however, the programs use different approaches when solving the minimization problem. SQUEEZE/MACIM perform global stochastic minimization by simulated annealing whereas BSMEM uses a local gradient-based approach. Despite the differences in implementation, the images produced by these packages are in remarkable agreement. This is proof that given the same data, the software frequently converge to the same solution. Because of this, we present the SQUEEZE total variation regularization images here and other SQUEEZE and BSMEM images as supplementary material.

To access the presence of artifacts in our image reconstruction method, we adopted a pragmatic approach in which (1) we find the best-fit model from our minimization process, (2) sample the model using the same UV coverage as the original to create synthetic data, (3) redistribute the nominal values in the synthetic data using the uncertainties from the real data, and (4) reconstruct the simulated model image using the same methods as the real data. Steps two and three were performed using *oifits-sim*.[13] The three images (real, model, and simulated model) are then compared qualitatively. Features present in the model that are also present in the real and simulated model images are likely true. Conversely, features seen in the real or simulated model image that are not present in the model are likely artifacts of the reconstruction process. Finally, features present in the real image but not explained otherwise may be real, but warrant further investigation.

5. RESULTS

5.1. Model Selection for the F-star's Limb Darkening Law

We have used the four post-eclipse CHARA-MIRC observations to compare seven different limb darkening laws for the F-star. As seen in Table 3, the uniform disk model is always a poor fit to the data compared to the limb darkening models. In all but one epoch, the quadratic limb darkening law was found to be a better fit to the interferometric data than other models. On 2011 October 10, the two-parameter law described in Fields et al. (2003) was a better fit.

It would appear that the quadratic limb darkening law is most appropriate; however, an inspection of the fits reveals that all models predict essentially the same visibility function. Interestingly, all models also predict significantly lower flux at the limb than is implied by either plane parallel or spherical stellar atmosphere codes. We verified that the *SIMTOI* results matched LitPro's analytical models, therefore, it is unlikely that this effect is fictitious. We have noticed small, few degree, non-

zero closure phases and two epochs where the location of the first visibility null differs between baselines. Thus it is possible that the F-star may be slightly oblate or have surface features. We will explore these possibilities in greater detail in a future publication. Because it is simple and can reproduce the data, we pragmatically adopted the power-law limb darkening law to represent the F-star in this work. The mean out-of-eclipse diameter and limb darkening coefficient are 2.22 ± 0.09 mas and 0.50 ± 0.26, respectively. This range of values compares favorably with published diameters from the NPOI (θ_{UDD} 2.18 ± 0.05 mas at 0.5–0.85 μm, Nordgren et al. 2001), the Mark III (limb darkened diameter, θ_{LDD}, 1.888–2.136 mas at 0.4–0.8 μm, Mozurkewich et al. 2003), and PTI (θ_{UDD} 2.27 ± 0.11 mas at 2.2 μm, Stencel et al. 2008) interferometers.

5.2. Initial Estimation of the Orbital Parameters

Using the equations in Section 3.4, we have estimated the orbital semimajor axis. Assuming $T = 9896 \pm 1.6$ days (Stefanik et al. 2010), the H-band ingress time 145 ± 15 days (Hopkins 2012), and a circular orbit, we estimate $\alpha_T = \alpha_1 + \alpha_2 \sim 24 \pm 2.6$ mas where α_1 and α_2 are the semimajor axes of the F-star and disk with respect to the system's center of mass. In the elliptical case, the spectroscopic elements from Stefanik et al. (2010) and Chadima et al. (2010) orbital elements yield nearly identical results of $\alpha_T \sim 31 \pm 3.7$ and 33 ± 4.5 mas, respectively. The dominant source of uncertainty in these values comes from the $\sim 10\%$ errors in ω and t_{ingress}. Recognizing estimates for the F-star's contribution to α_T are some 13 24 mas (Strand 1959; van de Kamp 1978; Heintz & Cantor 1994), we establish bounds of $13 < \alpha_T < 38$ mas for our minimization. A non-equatorial intersection, as seen in our previous work (Kloppenborg et al. 2010), will strictly decrease the upper bound on α_T.

Next, we estimated Ω by fitting the in-eclipse CHARA-MIRC data with a model consisting of a circular F-star with power-law limb darkening and cylindrical disk. We set $\alpha_T = 31$ mas and $r_{\mathrm{disk}} = 10$ mas while permitting the stellar and orbital inclination parameters to remain free. An average of $\Omega = 296 \pm 3$ deg was obtained from the six totality epochs.

5.3. Disk Model Selection via Multi-epoch Minimization

From the aforementioned disk models, we created eight variants. The geometric models are (1) a hard-edged cylinder, and three variants with power-law transparency in (2) both radius and height, (3) height only, and (4) radius only. The models from astrophysical density distributions are (5) a Pascucci et al. disk and (6) an Andrews et al. disk. Although not supported by the interferometric images, we decided to test for the central clearing hypothesis (c.f. Ferluga 1990, and references therein) and created (7) a Pascucci et al. disk with a variable inner radius. Finally we test whether the Kemp et al. (1986) polarization model by creating (8) a Pascucci et al. disk that may be tilted out of the orbital plane.

Using the *MultiNest* minimizer, we derived log Z estimates by simultaneously fitting each model to a subset of the H-band photometric data (consisting of 200 observations spaced at approximately equal intervals throughout the eclipse) and six interferometric epochs from CHARA-MIRC (2009-11, 2009-12, 2010-08, 2010-11, 2011-01, and 2011-09-18). The best-fit parameters, posterior odds ratio ($\Delta \log R$), and average χ^2 values for each model are shown in Table 5. The $\Delta \log R$

---

[13] Oifits sim: https://github.com/bkloppenborg/oifits_sim

Table 3
Posterior Odds Ratios ($\Delta \log R$) Relative to the Uniform Disk Model

	Posterior Odds Ratio ($\Delta \log R$, See Section 3.1)					
Epoch	Claret (2000)	Fields et al. (2003)	Logarithmic	Power Law[a]	Quadratic	Square Root
2011 09 18	9504	9518	9515	9506	9545	9506
2011 09 24	1954	1949	1959	1956	1971	1954
2011 10 10	2568	2615	2560	2561	2560	2558
2011 11 03	6151	5900	6165	6166	6227	6134

Note.
[a] Although there is slight evidence in favor of the quadratic limb darkening law, visual inspection of the visibility data shows no significant difference between it and the power law limb darkening that we pragmatically adopted in this work.

values indicate that model 8 (the tilted Pascucci disk) provides the best simultaneous fit to the data and was therefore adopted for the remainder of our work.

We have rendered the best-fit version of each disk model in Figure 2. With the exception of the cylindrical disk, all disk models have a characteristic size of ∼6 mas radius and ∼0.75 mas height before becoming optically thin. Plots of the corresponding H-band photometry in Figure 3 show that although the disk models appear physically different, they all do a reasonable job reproducing the global properties of the light curve. This clearly demonstrates that reproducing the photometry is a necessary, but not sufficient condition to prove the validity of any particular disk model. We note that none of these symmetric disk models are capable of reproducing all of the photometric features seen during the eclipse.

Using model 7 (a Pascucci disk with a variable inner radius), we test the notion that the disk's central clearing is responsible for the alleged mid-eclipse brightening. We find that the disk remains edge-on, but has an inner radius of some 3.8 mas. This implies that the inner 60% of the disk could be devoid of any opaque material. Despite this fact, the impact on the light curve is minimal. Given the geometry of the eclipse, light penetrating the central clearing cannot be responsible for any mid-eclipse brightening. We will discuss this result in greater detail in Section 6.

5.4. Bootstrapping and Aggregate Statistics

The photometry predicted by the symmetric disk models creates an interesting corollary: if one assumes the disk is symmetric, one may immediately conclude, to the contrary, that the disk must be asymmetric because the residuals between the observed and predicted photometry far exceed the F-star's $\Delta H \sim 0.05$ mag variations seen outside of eclipse. We tested this asymmetric conjecture by performing several single-epoch MultiNest minimizations to the in-eclipse MIRC data. We created three additional disk models which (a) forced the disk to reside in the orbital plane, (b) tilted the disk out of the orbital plane at a fixed angle, and (c) permitted both the position and inclination of the disk with respect to the orbital plane to vary. We find that the disk is tilted out of the orbital plane by less than 4° (1.33 ± 0.67 deg with rejection of one outlier) and has significant variations in structure (see Table 9).

To derive statistical uncertainties and simulated photometry we used the best-fit values from the aforementioned minimizations as starting points and bootstrapped each interferometric epoch 10,000 times. During each bootstrap we dynamically recalibrated the data using the uncertainty distribution of the calibrator. Then we created a new realization of the data using

Table 4
A Summary of all Parameters Used in the Modeling Process

Parameter	Range	Units	Description
F star parameters			
θ_{UDD}	1 3	mas	Uniform disk diameter
θ_{LDD}	1 3	mas	Limb darkened disk diameter
α_{LDD}	0 1		Power law limb darkening coefficient
Geometric disk models			
r_{in}	0	mas	Inner radius
r_{out}	1 30	mas	Outer radius
h_{disk}	0 5	mas	Height
α	5 20		Radial exponent
β	0.1 5		Height exponent
Astrophysical density disk models			
$\kappa_0 \rho_0$	3000 10,000		Characteristic opacity
α	5 20		Radial exponent (Pascucci model)
β	0.1 5		Height exponent (Pascucci model)
γ	0.001 20		Radial exponent (Andrews model)
h_c	0.001 20	mas	Disk scale height
r_c	1 4	mas	Disk scale radius
i_{disk}	±10	deg	Disk inclination
Ω_{disk}	±10	deg	Disk position angle
Orbital parameters[a]			
e	0.227 ± 0.01		Eccentricy
i	70 110	deg	Inclination
ω	39.2 ± 3.4	deg	Longitude of periastron
P	$9{,}896 \pm 1.6$	day	Period
Ω	90 145 and 270 325	deg	Position Angle
$\alpha_T, \alpha_1, \alpha_2$	$13 < \alpha_T < 38$	mas	Semi major axis (total, F star, disk)
T	$2{,}434{,}723 \pm 80$	days	Time of periastron

Note.
[a] e, ω, P, and T from Stefanik et al. (2010).

the measured uncertainties, taking into account any known correlations (i.e., as seen in spectrally dispersed visibilities) in the data when required. The results of this effort are shown in Table 6 with a subset of the results plotted in Figure 4.

By inspection of Table 6, one can see that the angular diameter and limb darkening profile of the F-star are largely consistent within 1σ. This implies that there are no egregious systematic calibration errors between our data sets. Furthermore, these results show that there has been no secular change to the F-star's diameter over the last 14 years. However, our observations are not sufficiently precise to definitively exclude

Table 5
Bayes Factors Relative to the Cylinder Model and Average Reduced χ^2 for the Six Disk Models Described in the Section 3.3

Name	Model[a]	Orbit		Disk										Fit Information				
		α_T (mas)	i (deg)	r_{in} (mas)	r_{out} (mas)	h (mas)	α	β	r_c (mas)	h_c (mas)	$\kappa\rho$ [b]	Ω_{disk} (deg)	i_{disk} (deg)	$\Delta \log R$	$\chi_r^2(H)$	$\overline{\chi_r^2}(V^2)$	$\overline{\chi_r^2}(T_{3A})$	$\overline{\chi_r^2}(T_{3\phi})$
Cylinder	1	21.7	88.4	0.0	4.85	0.54	...	...	...	...	...	...	...	0	260	10	12	48
Ringed Disk	2	27.0	88.7	0.0	7.20	0.71	0.13	1.64	...	...	...	...	...	63940	69	4.1	4.3	31
RingedDisk (only β)	3	27.5	88.8	0.0	6.39	0.79	...	0.02	...	...	...	...	...	59811	93	4.4	4.1	32
RingedDisk (only α)	4	27.5	88.8	0.0	7.40	0.70	0.11	...	...	...	...	...	...	63792	67	4.1	4.4	31
Pascucci Disk	5	33.0	89.0	0.0	...	...	11.11	1.75	2.39	0.029	6496	...	...	67058	50	3.8	4.1	30
Andrews Disk	6	33.0	89.0	0.0	...	...	11.14	1.74	2.48	0.032	5161	...	...	67110	49	3.8	4.1	31
Pascucci Disk w/ clearing	7	32.6	88.9	3.8	...	...	10.94	0.75	2.32	0.079	6667	...	...	67254	51	3.8	4.0	31
Tilted Pascucci Disk[c]	8	31.2	88.9	0.0	...	...	13.33	3.69	2.77	0.007	6287	0.02	2.98	68806	50	3.7	3.7	28

Notes.
[a] See Section 5.3 for model descriptions.
[b] The product $\kappa\rho$ was treated as a single quantity in our minimization process. see Section 5.3 for further details.
[c] Model 8 obtains the highest Bayes factor and is therefore adopted in this work.

the 0.6% year^{1} contraction rate suggested by Saitō & Kitamura (1986).

In the top panel of Figure 4 we plot the H-band photometry as observed, simulated from the symmetric model, and predicted from the bootstrap process described above. Not all of the photometric values are in perfect agreement, but this is expected as the photometry was not used as a constraint in the bootstrapping process. We note that a small change in disk structure can have a substantial impact on the observed photometry (e.g., a 0.1 mas difference in thickness, five times smaller than our resolution limit, results in $\Delta H \sim 0.1$ mag), thus the predicted photometry is in reasonable agreement.

In the bottom three panels of Figure 4, we plot the angular diameter, limb darkening coefficient, disk scale height, h_c, and height power-law exponent, β, as a function of time. The 1σ estimates for h_c and β from model 8 do not overlap well with the single-epoch bootstraps. This is likely due to the $\sim 1.6°$ difference in disk inclinations between the models. The changes in h_c and β (greater h_c, smaller β) indicate that the disk is more spatially extended in height before mid-eclipse than it is after mid-eclipse. Combined with the asymmetric evolution of several neutral absorption lines during eclipse (c.f. Lambert & Sawyer 1986; Leadbeater et al. 2012), the evidence suggests that the disk is not purely symmetric. We suspect that these features could be explained by asymmetric heating (c.f. Takeuti 2011) and sublimation of the disk on the side facing the F-star. Verifying this claim by hydrodynamical radiative transfer simulations is beyond the scope of this work.

Because of the limited UV coverage, the egress CHARA-CLIMB data was fit in conjunction with an interpolated photometric point. The result reveals that the F-star is similar in size, but the disk is more extended in the vertical direction than the CHARA-MIRC observations three months earlier would imply. This interpretation is supported by the appearance of the model-independent images (discussed below); however, we caution the reader that this may simply be an artifact of the limited UV coverage of this data set.

In Table 7, we show the aggregate statistics derived from single-epoch bootstrapping for each beam combiner. We believe these values represent the general characteristics of the system. In Table 8, we summarize these quantities for a variety of distance estimates for the system. Due to the large scatter of possible distances (0.5 4 kpc), we use only the nominal values and do not propagate any uncertainties from the distance measurements. We caution the reader that the aggregation of data to create Table 8 was performed without regard to either the wavelength of observation or any asymmetries we advocate exist. Hence, the outliers have biased and skewed the resulting value. We provide this last table to assist with the creation of a full radiative transfer model of the system including dust physics rather than provide a definitive measurement of the properties of the system.

5.5. Reconstructed Images and Artifacts

In Figure 5, we present the best-fit model and model-independent SQUEEZE reconstructions using the total variation regularizer. By following the qualitative comparison method discussed in Section 4, we may distinguish whether the features seen in these images are real signals or artifacts of the reconstruction process. A detailed discussion of this process, as well as BSMEM and other SQUEEZE reconstructions, can be found in the Appendix and extended Figures

A46 A52. Summarizing this account, the true features are as follows: (1) the dark lane in the F-star's southern hemisphere, interpreted to be the disk; (2) flux that appears on the far south west (or south east) edge of the F-star during ingress (egress); and (3) the presence or absence of the F-star's southern pole. Although the post-eclipse interferometric observations do feature small non-zero closure phases and photometry of the ϵ Aurigae system does show an intrinsic $\Delta V \sim 0.1$ mag photometric variation outside of eclipse, we presently regard any flux variations on the surface F-star as artifacts.

6. CONCLUSIONS AND DISCUSSION

We have analyzed 106 nights of interferometric observations provided by four beam combiners at three different interferometric facilities to derive properties of the F-star, determine previously unknown orbital elements, and access the global structures of the optically thick portion of the eclipsing disk. We have reconstructed a series of model-independent images using SQUEEZE and BSMEM programs with a variety of regularization functions. The images show that the F-star appears circular (round) and free of egregious asymmetries prior to and after the 2009 2011 eclipse. During the eclipse, most of the southern hemisphere on the F-star is obscured. The appearance and persistence of this feature lead us to confirm the Huang Lissauer disk hypothesis for the eclipse. During most of the epochs, the southern pole of the F-star is visible, thereby providing an opportunity to measure the thickness of the disk at sub-milliarcsecond resolution.

Our interferometric modeling efforts were complex: under a Bayesian framework, we tested the observations of the F-star against seven different analytic limb darkening prescriptions and differentiated between eight proposed disk models. The Bayes factors listed in Table 5 are all exceptionally large. After conducting a comprehensive over-view of *SIMTOI*'s rendering pipeline, *liboi*'s unit test framework, and our use of MultiNest, we found no mistakes in our implementation. Hence these values are either true, or there is some unforeseen systematic error for which or modeling process did not account. Nevertheless, we are confident that our best-fit model is indeed the most probable as it achieves the lowest reduced chi-squared estimate. The pre- and post-eclipse observations indicate that the F-star has remained at a more-or-less constant diameter for the last 14 years; however, our observations are not sufficiently precise to definitively exclude the 0.6% year^{1} contraction rate suggested by Saitō & Kitamura (1986). The average power-law limb darkening coefficient, ~ 0.5, is much higher than predicted for an F-type supergiant (~ 0.1–0.2). The presence of small, $<5°$, non-zero closure phases on the longest baselines in the post-eclipse observations, coupled with variations in radius and limb darkening seen during the eclipse, suggest that there may be convective cells or some other feature (e.g., spots) on the surface of the F-star. These features, if they exist, have only a minimal impact on our results.

We have simultaneously fit the disk models to a subset of the interferometric and photometric data. We find that the data can be adequately fit by a variety of models; however, the most consistent model was that of tilted disk derived from an astrophysical density distribution. The opaque region of the disk is seen nearly edge on and is remarkably uniform. These conclusions are supported by spectroscopic work by Griffin &
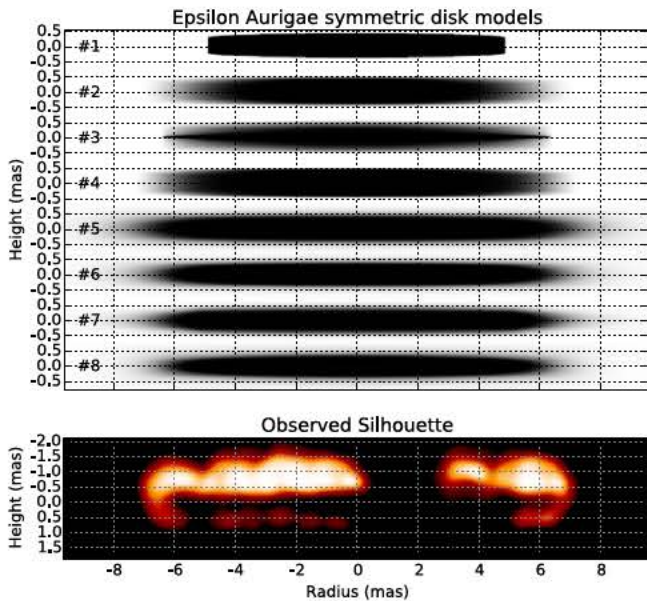
Figure 2. (Top) The eight best fit symmetric disk models resulting from a simultaneous minimization to both the photometric and interferometric data. The models are as described in Section 3.3. All models have been rotated in position angle, but otherwise appear as they would when occulting the F star's photosphere. Model #8 has the greatest evidence value and was adopted for the remainder of this work. (Bottom) The disk's silhouette created by aligning the individual SQUEEZE reconstructions with our orbital solution. See Appendix B for further details.
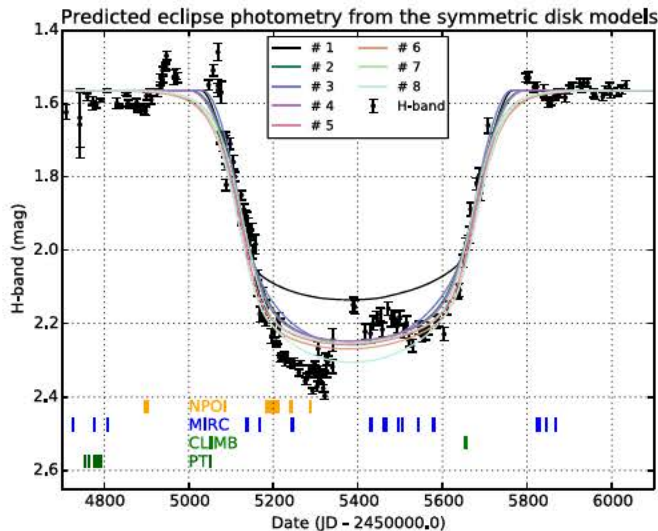

Figure 3. Observed and simulated H band photometry from the eight best fit symmetric disk models as a function of time. The four rows of tick marks at the bottom of the plot indicate the time of observation by the corresponding beam combiner. Tick marks appear thicker when successive nights of observations occurred. None of the symmetric disk models entirely reproduce all features of the light curve, implying that the disk is not symmetric. The F star's $\Delta H \sim 0.05$ mag out of eclipse variations are clearly seen at all phases of the eclipse.

Stencel (2013), who have shown the precise repetition of disk-related spectral features have not changed appreciably over the last century. Therefore, it is unlikely that the disk is significantly twisted or warped (Kumar 1987). We do, however, find evidence that the disk may be slightly tilted out of the orbital plane. If this is true, the difference between

our model and the Kemp et al. (1986) polarization result could be attributed to precession.

The thickness and inclination of the disk exclude the possibility that a the purported mid-eclipse brightening is caused by light penetrating a central clearing in the disk (cf. Wilson 1971) or the notion that a series of semi-transparent rings are responsible for the photometric variations seen during totality (cf. Ferluga 1990, 1989). We suggest that these light curve features, if true, have other physical causes. For example, a mid-eclipse brightening could be due to scattering above and below the plane of the disk (e.g., Budaj 2011; Muthumariappan & Parthasarathy 2012), perhaps in the same region responsible for the increase in He 10830 Å absorption (Stencel et al. 2011). Likewise, the manifestation of $\Delta V \sim 0.1$ mag variations during totality are probably orbitally excited non-radial pulsation of the F-star (Kloppenborg et al. 2012), rather than substructure in the disk.

Finally we predict that the secondary eclipse will occur between $\sim$JD 2,461,030$-$2,461,860 (2025 December 20 2028 March 29). We encourage a comprehensive photometric campaign during this time focusing on NIR, mid-IR, and far-IR observations to confirm this prediction.

APPENDIX A
IMAGE RECONSTRUCTION AND ARTIFACT DISCUSSION

In the following section, we elaborate on the image reconstruction and artifact detection process for all epochs. We present the best-fit SIMTOI model and reconstructed with SQUEEZE and BSMEM. All images are rendered with North up and east to the left. The 0.5 mas H-band or 0.7 mas K-band resolution limit of the data is indicated by the circle in the lower left-hand corner of the model image.

The SQUEEZE reconstructions were conducted using the Laplacian (abbreviated LA), Total Variation (abbreviated TV), and L0-norm (abbreviated L0) regularizers. Images were reconstructed in a grid with regularizer weights ranging from 0.1 100,000 in semi-logarithmic steps. The images with the lowest reduced chi-squared were selected for presentation. Most of the epochs were reconstructed from a Dirac

Table 6
Bootstrapped Nominal Values and Uncertainties for Model 8 With a Fixed Tilt Evaluated on a Per epoch Basis Subject to Only the Interferometric Data

Data set	$N(V^2)$	$N(T_3)$	$N(UV)$	Effective JD	F-star			Disk					Statistical Information				Notes
					θ_{UDD} (mas)	θ_{LDD} (mas)	α_{LDD} ($\times 10^{-2}$)	$\kappa\rho$ ($\times 10^{-2}$)	r_c (mas)	h_c (mas)	α	β^a	χ^2_r	$\chi^2_r(V^2)$	$\chi^2_r(T_{3A})$	$\chi^2_r(T_{3\phi})$	
1997-10-22-PTI	14	...	16	2450744.0200	2.43 ± 0.29	...	...	...	...	...	...	...	0.38	0.38	...	...	...
1998-11-07-PTI	66	...	69	2450761.9500	2.13 ± 0.28	...	...	...	...	...	...	...	0.27	0.27	...	...	Distribution not well constrained
1997-11-09-PTI	20	...	21	2451124.9500	2.78 ± 0.15	...	...	...	...	...	...	...	2.21	2.21	...	...	...
1998-11-25-PTI	10	...	11	2451142.9400	1.93 ± 0.44	...	...	...	...	...	...	...	0.78	0.78	...	...	Distribution well constrained. HD 30823 sole calibrator this night. Perhaps calibrator diameter over-estimated?
1998-11-26-PTI	5	...	5	2451143.9300	2.06 ± 0.53	...	...	...	...	...	...	...	0.53	0.53	...	...	Distriubtion poorly constrained. Nominal value matches best-fit MultiNest estimate.
2006-02-NPOI	540	135	544	2453791.7434	2.09 ± 0.06	...	...	...	...	...	...	...	2.35	2.65	2.00	1.49	...
2007-03-NPOI	660	330	966	2454173.6316	...	$2.28^{+0.07}_{-0.02}$	$0.42^{+0.23}_{-0.05}$	...	...	...	...	...	2.28	0.90	1.67	5.67	...
2007-10-19-PTI	100	...	104	2454392.9900	2.13 ± 0.13	...	...	...	...	...	...	...	0.59	0.59	...	...	...
2007-10-20-PTI	81	...	84	2454393.9700	2.08 ± 0.14	...	...	...	...	...	...	...	0.18	0.18	...	...	...
2007-10-21-PTI	40	...	43	2454394.9800	2.16 ± 0.24	...	...	...	...	...	...	...	1.35	1.35	...	...	...
2007-11-27-PTI	20	...	22	2454431.8500	2.55 ± 0.32	...	...	...	...	...	...	...	2.16	2.16	...	...	Distribution not constrained, highly skewed toward higher values.
2007-12-23-PTI	5	...	5	2454457.7800	2.09 ± 0.43	...	...	...	...	...	...	...	0.68	0.68	...	...	...
2007-12-24-PTI	35	...	39	2454458.7500	2.45 ± 0.26	...	...	...	...	...	...	...	1.75	1.75	...	...	...
2008-02-17-PTI	10	...	10	2454513.6400	1.75 ± 0.33	...	...	...	...	...	...	...	3.22	3.22	...	...	Distribution is well constrained. Bad calibration?
2008-02-18-PTI	25	...	27	2454514.6500	2.17 ± 0.34	...	...	...	...	...	...	...	1.77	1.77	...	...	...

Table 6
(Continued)

Data set	$N(V^2)$	$N(T_3)$	$N(UV)$	Effective JD	F-star			Disk					Statistical Information				Notes
					θ_{UDD} (mas)	θ_{LDD} (mas)	α_{LDD} ($\times 10^{-2}$)	$\kappa\rho$ ($\times 10^{-2}$)	r_c (mas)	h_c (mas)	α	β^{a}	χ^2_r	$\chi^2_r(V^2)$	$\chi^2_r(T_{3A})$	$\chi^2_r(T_{3\phi})$	
2008-09-CHARA-MIRC	23	8	50	2454729.0153	...	$2.28^{+0.08}_{-0.08}$	$0.69^{+0.20}_{-0.20}$	...	...	...	...	...	1.91	2.46	1.94	0.29	Errors limited by calibrator uncertainty
2008-10-17-PTI	65	...	69	2454757.0000	2.37 ± 0.20	...	...	...	...	...	...	...	5.71	5.71	...	...	...
2008-10-26-PTI	80	...	84	2454765.9800	2.01 ± 0.15	...	...	...	...	...	...	...	0.88	0.88	...	...	...
2008-11-CHARA-MIRC	138	76	268	2454778.5967	...	$2.22^{+0.06}_{-0.06}$	$0.39^{+0.12}_{-0.12}$	...	...	...	...	...	3.81	4.59	3.24	2.96	Errors limited by calibrator uncertainty
2008-11-08-PTI	10	...	11	2454778.8700	2.17 ± 0.40	...	...	...	...	...	...	...	0.08	0.08	...	...	...
2008-11-09-PTI	20	...	21	2454779.8700	2.34 ± 0.49	...	...	...	...	...	...	...	2.18	2.18	...	...	Distribution not constrained and highly skewed toward higher values. Bad calibration?
2008-11-16-PTI	10	...	10	2454786.8700	...	...	...	...	...	...	...	...	...	...	...	...	...
2008-11-22-PTI	50	...	52	2454792.8200	2.30 ± 0.23	...	...	...	...	...	...	...	1.32	1.32	...	...	...
2008-12-CHARA-MIRC	38	8	65	2454810.8249	...	$2.36^{+0.06}_{-0.06}$	$0.80^{+0.17}_{-0.17}$	...	...	...	...	...	3.67	4.03	5.42	0.23	Errors limited by calibrator uncertainty
2009-03-NPOI	840	420	1225	2454898.6326	...	$2.16^{+0.07}_{-0.02}$	$0.37^{+0.25}_{-0.04}$	...	...	...	...	...	1.85	1.65	1.29	2.80	...
2009-11-CHARA-MIRC	1091	672	2575	2455138.9326	...	$2.29^{+0.02}_{-0.03}$	$0.62^{+0.08}_{-0.10}$	6329^{+2038}_{-2038}	$1.79^{+0.02}_{-0.02}$	$2.57^{+0.40}_{-0.40}$	$9.19^{+0.04}_{-0.06}$	$1.56^{+0.12}_{-0.10}$	4.01	2.64	0.00	8.57	...
2009-12-CHARA-MIRC	730	392	1662	2455169.0375	...	$2.28^{+0.04}_{-0.04}$	$1.00^{+0.11}_{-0.12}$	6842^{+2009}_{-2009}	$3.72^{+0.07}_{-0.07}$	$12.18^{+0.50}_{-1.00}$	$19.94^{+0.01}_{-0.03}$	$0.10^{+0.28}_{-0.02}$	9.26	4.08	3.77	24.39	...
2009-12-NPOI	290	29	293	2455185.6210	...	$2.05^{+0.21}_{-0.04}$	$0.72^{+0.28}_{-0.20}$	7007^{+1847}_{-1847}	$3.23^{+0.22}_{-0.03}$	$6.70^{+8.50}_{-4.10}$	$16.72^{+0.04}_{-0.06}$	$0.92^{+0.21}_{-0.16}$	2.14	2.20	1.89	1.73	Visibities at short baselines are much higher than CHARA model would predict.
2010-01 AB-NPOI	3324	1376	4444	2455205.5082	...	$2.24^{+0.03}_{-0.02}$	$0.76^{+0.14}_{-0.07}$	6211^{+1690}_{-1690}	$2.97^{+0.08}_{-0.06}$	$4.10^{+0.30}_{-0.30}$	$17.84^{+0.02}_{-0.02}$	$2.43^{+0.07}_{-0.02}$	1.23	1.61	1.21	0.33	Disk r_c is clearly bimodal
2010-02-NPOI	810	265	814	2455243.1816	...	$2.37^{+0.10}_{-0.10}$	$0.62^{+0.24}_{-0.24}$	6219^{+2000}_{-2000}	...	$10.70^{+1.30}_{-1.30}$	...	$0.70^{+0.23}_{-0.23}$	1.42	1.47	1.81	0.87	...
2010-02-CHARA-MIRC	96	64	236	2455245.7444	...	$2.01^{+0.04}_{-0.04}$	$0.21^{+0.13}_{-0.13}$	3075^{+1600}_{-1600}	...	$13.14^{+0.50}_{-0.50}$	...	$0.55^{+0.11}_{-0.11}$	6.88	1.64	1.18	20.45	Interferometry + Photometry. Statistics from MultiNest distribution.

Table 6
(Continued)

Data set	$N(V^2)$	$N(T_3)$	$N(UV)$	Effective JD	F-star			Disk					Statistical Information				Notes
					θ_{UDD} (mas)	θ_{LDD} (mas)	α_{LDD} ($\times 10^{-2}$)	$\kappa\rho$ ($\times 10^{-2}$)	r_c (mas)	h_c (mas)	α	β^a	χ^2_r	$\chi^2_r(V^2)$	$\chi^2_r(T_{3A})$	$\chi^2_r(T_{3\phi})$	
2010-04-NPOI	15	0	15	2455289.6026	...	$2.33^{+0.28}_{-0.28}$	$0.56^{+0.24}_{-0.24}$	6500^{+2000}_{-2000}	...	$11.50^{+7.70}_{-7.70}$	...	$0.88^{+1.05}_{-1.05}$	0.53	0.53	0.00	0.00	...
2010-08-CHARA-MIRC	960	640	2164	2455430.5170	...	$2.33^{+0.04}_{-0.04}$	$0.74^{+0.09}_{-0.11}$	9901^{+1334}_{-1334}	...	$1.27^{+0.10}_{-0.10}$	...	$3.75^{+0.07}_{-0.12}$	10.74	3.97	3.90	27.74	...
2010-09-CHARA-MIRC	1176	728	3020	2455464.4883	...	$2.37^{+0.03}_{-0.02}$	$0.73^{+0.06}_{-0.04}$	5944^{+1888}_{-1888}	...	$2.35^{+0.20}_{-0.10}$	...	$3.11^{+0.10}_{-0.08}$	3.38	1.96	1.98	7.07	...
2010-10-CHARA-MIRC	288	152	732	2455496.4319	...	$2.26^{+0.03}_{-0.03}$	$0.62^{+0.08}_{-0.08}$	6629^{+1973}_{-1973}	...	$1.47^{+0.80}_{-0.10}$	...	$3.56^{+0.18}_{-0.62}$	1.77	1.31	0.77	3.67	...
2010-11-CHARA-MIRC	288	192	763	2455505.4193	...	$2.18^{+0.01}_{-0.01}$	$0.11^{+0.05}_{-0.03}$	3720^{+1817}_{-1817}	...	$9.66^{+0.20}_{-0.20}$	...	$0.40^{+0.11}_{-0.07}$	4.64	2.93	1.16	10.71	...
2010-12-CHARA-MIRC	191	112	475	2455543.7059	...	$2.22^{+0.04}_{-0.03}$	$0.31^{+0.10}_{-0.09}$	5548^{+1985}_{-1985}	...	$0.72^{+0.10}_{-0.10}$	...	$4.71^{+0.28}_{-0.28}$	5.72	2.29	1.36	15.92	...
2011-01-CHARA-MIRC	310	182	860	2455580.2465	...	$2.18^{+0.02}_{-0.02}$	$0.25^{+0.04}_{-0.04}$	3013^{+1838}_{-1838}	...	$4.94^{+1.10}_{-0.20}$	...	$1.84^{+0.16}_{-0.52}$	5.01	2.57	1.36	12.83	...
2011-04-CHARA-CLIMB	41	14	45	2455655.0673	...	$2.33^{+0.06}_{-0.06}$	$0.33^{+0.48}_{-0.48}$	6100^{+2000}_{-2000}	$3.48^{+0.30}_{-0.30}$	$13.20^{+3.80}_{-3.80}$	$18.55^{+1.96}_{-1.96}$	$0.64^{+0.50}_{-0.50}$	3.23	4.06	1.04	2.97	...
2011-09-18-CHARA-MIRC	201	240	756	2455823.0305	...	$2.25^{+0.02}_{-0.04}$	$0.62^{+0.06}_{-0.10}$	...	...	...	...	...	5.06	3.55	3.02	8.37	...
2011-09-24-CHARA-MIRC	120	160	394	2455829.0277	...	$2.17^{+0.03}_{-0.03}$	$0.36^{+0.06}_{-0.07}$	...	...	...	...	...	5.40	3.32	1.67	10.69	...
2011-10-10-CHARA-MIRC	400	480	1412	2455844.9422	...	$2.12^{+0.04}_{-0.05}$	$0.34^{+0.11}_{-0.12}$	...	...	...	...	...	16.97	5.49	6.82	36.70	...
2011-11-03-CHARA-MIRC	831	1119	2677	2455868.8509	...	$2.25^{+0.03}_{-0.07}$	$0.57^{+0.08}_{-0.17}$	...	...	...	...	...	12.14	5.64	7.21	21.90	...

Note.
[a] The changes seen in height power, β, hint that there may be some asymmetric structure in the disk.
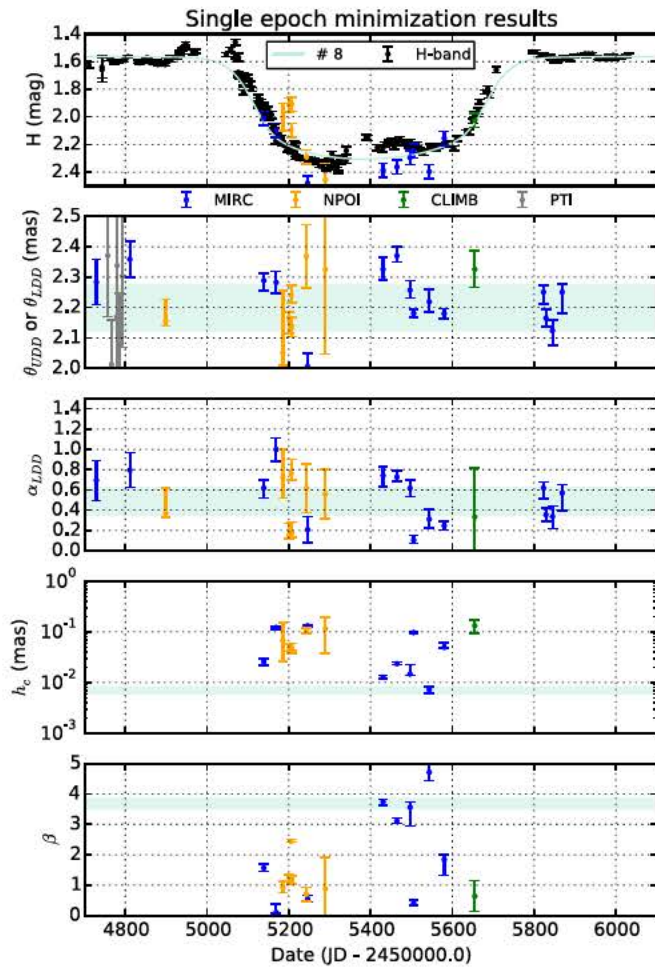
Figure 4. Results of single epoch minimizations to the interferometric (and in two cases photometric) data. Top: the observed and predicted H band photometry as a function of time. Superimposed is the best fit symmetric disk model (#8) and predicted H band magnitudes from the single epoch fits. Bottom: the best fit F star diameter (limb darkened or uniform); limb darkening coefficient; disk scale height; and disk radial exponent, β, as a function of time. The horizontal bands denote the 1σ limits on the parameters from model eight. The diameter of the F star is largely consistent, regardless of the wavelength of observation. This indicates there is not an egregious systematic calibration error between the different interferometric facilities.

starting image. However, the sparse UV coverage in the 2008-11, 2010-02, and 2011-04 mandated we use the best- fit model images to initialize the flux distribution. SQUEEZE was executed with 50 threads with 500 realizations each.

All BSMEM reconstructions were performed using flat priors and a 1.4 mas diameter Gaussian for entropy estimation. We have used the "full" elliptical approximation for the bispectra uncertainties (see BSMEM documentation for details) which we found dramatically suppress reconstruction artifacts.

A.1. 2008-11

Figure A46 shows the resulting model and image from this set of two four-telescope MIRC observations that were taken at nearly the same hour angle. The image reconstruction in this epoch is quite poor when compared with later epochs. By inspection of the SED (Hoard et al. 2012, 2010) we know that the F-star is the dominant source of flux in the H band, hence we interpret this to be an image of the F-star. All of the images show that the flux is mostly constrained within the

bounds of the best-fit model. The model-independent image shows the star as approximately round with some surface features. These features are mostly replicated in the model-independent reconstruction from the synthetic data, hence the non-circular structure and small photometric variations seen on the F-star are artifacts of the reconstruction process. Therefore the F-star before the eclipse does not appear to have any egregious asymmetries which might interfere with later observations.

A.2. 2009-11

In Figure A47, we show the best-fit model and model-independent images reconstructed from this eclipse ingress phase epoch. For reasons discussed above (and in greater detail in Kloppenborg et al. 2010), we again interpret the bright source to be the F-star and the dark region occuring in the southern half of the image as the disk intruding into the line of sight. We are not aware of any evidence which suggests the F-stars rotation is misaligned to the binary's orbit, hence we shall call the un-eclipsed portion of the F-star the "northern hemisphere." Likewise, we will refer to the (mostly) eclipsed portion as the "southern hemisphere." The North pole of the F-star would be located at a position angle of $\sim 26°$.

By comparing the best-fit model from SIMTOI to the sampled model reconstruction, we may qualitatively access the presence of artifacts in the image. The dark spot in the northern hemisphere and two bright spots in the east/west near the limb appear to be artifacts. The straight edges along the perimeter of the F-star are a common artifact caused by the UV coverage of the data set.

Despite the large number of artifacts, several real features may be discerned. For example, the southern pole is seen in the real image, model, and synthetic reconstruction; hence we feel this feature is real. Likewise, the small amount of flux seen on the western edge of the disk intrusion is also real.

A.3. 2009-12

The best-fit model and reconstructed images of this second ingress epcoh are shown in Figure A48. This data has excellent UV coverage and appears similar, in many regards, to the 2009-11 epoch. Like previous observations, the straight-edge appearance of the F-star is an artifact of the UV coverage. It is probable that the spots seen in the northern hemisphere of the F-star are also artifacts.

The southern pole again appears quite strong in the real image, model, and synthetic reconstruction, implying this feature is likely real. For the same reason, we regard the small quantity of flux at the west edge of the disk intrusion to be a real feature rather than an artifact of the reconstruction process.

A.4. 2010-02

The UV coverage at this epoch is extremely poor, consisting of two four-telescope observation with MIRC. Hence the model-independent images shown in Figure A49 are difficult to interpret without information garnered from the model and H-band photometry. Both the model and images imply that the entire southern hemisphere and a small fraction of the northern hemisphere are covered. This conclusion is supported, at least circumstantially, by the H-band photometry being at its faintest at this time. The appearance of bright spots in the northern hemisphere is most likely caused by limited UV coverage or

Table 7
Aggregate Statistics for all Interferometric Data with Uncertainties Determined from the Maximum of the Upper/Lower
Averaged Bootstrapped Uncertainties or the Standard Deviation of the Nominal Values

Quantity	Units	NPOI (V)	MIRC (H)	CLIMB (K)	PTI (K)
Quantity		NPOI (V)	MIRC (H)	CLIMB (K)	PTI (K)
θ_{UDD}	(mas)	2.09 ± 0.06	2.10 ± 0.15		2.22 ± 0.53
θ_{LDD}	(mas)	2.21 ± 0.28	2.22 ± 0.09	2.33 ± 0.06	…
α_{LDD}		0.47 ± 0.28	0.50 ± 0.26	0.33 ± 0.48	…
Ω_{disk}	(deg)		1.30 ± 0.67		…
i_{disk}	(deg)		89.49 ± 1.03		…
$\kappa\rho$[a]		6676 ± 2000	5667 ± 2188	6100 ± 2000	…
r_c	(mas)	3.10 ± 0.22	2.76 ± 1.36	3.48 ± 0.30	…
h_c	(mas)	0.07 ± 0.09	0.05 ± 0.05	0.13 ± 0.04	…
α		17.28 ± 0.79	14.56 ± 7.60	18.55 ± 1.96	…
β		1.23 ± 1.05	2.18 ± 1.67	0.64 ± 0.50	…

Notes. Orbital values of $\Omega = 297.60 \pm 0.06$ (deg), $i = 88.89 \pm 0.03$ (deg), and $\alpha_T = 31.2 \pm 0.9$ (mas) were used in these models.
[a] Not well constrained.

Table 8
Representative[a] Linear Equivalent of our Results if the System were at Various Distances in Literature

Quantity	This work		Nominal distance estimates (pc)					Linear units
			600[b,c]	653[d]	737[e]	1000[f]	1500[g]	
Ω	297 ± 3	(deg)						
i	89 ± 1	(deg)						
$\alpha_T = \alpha_1 + \alpha_2$	31 ± 3	(mas)	18.72 ± 1.80	20.37 ± 1.96	22.99 ± 2.21	31.20 ± 3.00	46.80 ± 4.50	(AU)
F star Radius	1.11 ± 0.05	(mas)	143.25 ± 5.81	155.90 ± 6.32	175.96 ± 7.13	238.75 ± 9.68	358.13 ± 14.52	($R_{\odot}$)
F star LDD coeff	0.50 ± 0.26							
Disk scale Height (h_c)	1.038 ± 0.139	(mas)	0.03 ± 0.03	0.03 ± 0.03	0.04 ± 0.04	0.05 ± 0.05	0.07 ± 0.07	(AU)
Disk scale radius (r_c)	7.416 ± 0.276	(mas)	1.66 ± 0.82	1.80 ± 0.89	2.03 ± 1.00	2.76 ± 1.36	4.14 ± 2.04	(AU)

Notes. These values average over all interferometric epochs. Therefore, these estimates are biased and are skewed by the outliers in Table 6.
[a] We caution the reader that this aggregation of data is performed in a wavelength and model agnostic fashion. Thus, any asymmetries in the system, which we argue exist, have biased the values quoted here. These values are supplied to ease the creation of a radiative transfer model including dust physics. We do not advocate that these values be quoted elsewhere.
[b] van de Kamp (1978).
[c] Heintz & Cantor (1994).
[d] van Leeuwen (2008).
[e] Kloppenborg (2012).
[f] Strand (1959).
[g] Guinan et al. (2012).

the reconstruction process, rather than any real surface flux variations on the F-star. The model independent and synthetic images agree quite well about the over-all appearance of the F-star during this epoch.

A.5. 2010-08 / 2010-09 / 2010-10 / 2010-11 / 2010-12 / 2011-01

The qualitative appearance of these epochs is quite similar (see Figure A50), hence they will be discussed in aggregate. The obscuration by the disk remains remarkably consistent across five months of observations. The occasional spot in the F-stars northern hemisphere, scalloped edge of the disk along the F-stars equator, and flux variations along the F-stars equator are frequently seen in the real data and synthetic reconstructions, hence these are likely artifacts. The southern pole has reappeared. It appears in the real image, model, and synthetic image therefore we regard this as a true feature in the image.

It is important to note that the mid-eclipse observation (2010-08) shows the disk as entirely opaque. Hence mid-eclipse brightening hypotheses, which rely on a large opening

in the disk, are unlikely. Likewise, although photometric variations were seen during this phase of the eclipse, no significant flux variations were seen within the disk plane, hence the photometric variations are not likely a result of flux penetrating semi-transparent gaps in the disk's midplane.

A.6. 2011-04

In Figure A51 we present the only interferometric images of the ϵ Aurigae during the egress phase and the first image created with data taken by the CLIMB beam combiner. Unlike all other data sets, the L0-norm images also required the use of the uniform disk regularizer in SQUEEZE. These model-independent K-band images show that a portion of the F-star's south east edge is no longer obscured by the disk. This notion is in excellent agreement with the SIMTOI model and observed photometry (e.g., see Figure 4). A bulk comparison of the reconstructed model versus real data implies that the large concentration of flux in the F-star's northern hemisphere is probably an artifact, whereas the small crescent of the F-star seen in the east is real.

Table 9
Best fit Values and Statistical Information for Single epoch MultiNest Minimizations Involving Three Variants[a] of the Tilted Pascucci Disk Model (Model 8) The Posterior Odds Ratio ($\Delta \log R$) is Relative to the Pascucci Zero tilt Disk Model

	F star		Disk							Statistical Information				
	$\theta_{\rm LDD}$(mas)	$\alpha_{\rm LDD}$	$i_{\rm disk}$(deg)	$\Omega_{\rm disk}$(deg)	α	r_c(mas)	β	h_c(mas)	$\kappa\rho$	$\Delta \log R$	χ^2_r	$\chi^2_r(V^2)$	$\chi^2_r(T_{3A})$	$\chi^2_r(T_{3\phi})$
Model: Pascucci zero tilt														
2009 11	2.30	0.63	...	...	9.19	1.87	1.67	0.023	4708	...	4.92	4.23	2.62	8.34
2009 12	2.28	1.00	...	...	19.95	3.71	0.10	0.118	7046	...	9.39	4.00	3.78	25.02
2010 02	2.43	0.98	...	...	...	...	0.75	0.173	3046	...	3.47	2.83	3.26	4.66
2010 08	2.33	0.74	...	...	...	...	3.78	0.011	4349	...	10.25	4.00	3.69	26.18
2010 09	2.37	0.72	...	...	...	...	3.00	0.021	3336	...	3.24	1.98	2.05	6.48
2010 10	2.29	0.66	...	...	...	...	4.20	0.007	5569	...	1.78	1.33	0.91	3.49
2010 11	2.18	0.10	...	...	...	...	0.36	0.093	3106	...	4.80	2.91	1.14	11.29
2010 12	2.29	0.41	...	...	...	...	4.83	0.005	3726	...	4.94	2.92	1.49	11.84
2011 01	2.13	0.18	...	...	...	...	3.05	0.015	3030	...	5.73	3.31	1.86	13.71
Average	2.29 ± 0.09	0.60 ± 0.32	0	0	14.57 ± 7.61	2.79 ± 1.30	2.41 ± 1.75	0.052 ± 0.061	4215 ± 1373	...	5.39	3.06	2.31	12.34
Model: Pascucci fixed tilt														
2009 11	2.29	0.62	...	...	9.19	1.79	1.56	0.026	6329	37	4.91	3.98	2.64	8.69
2009 12	2.28	1.00	...	...	19.94	3.72	0.10	0.122	6842	119	9.22	3.93	3.63	24.66
2010 02	2.43	0.99	...	...	...	...	0.72	0.179	5	296	3.53	2.92	3.39	4.59
2010 08	2.33	0.74	...	...	...	...	3.35	0.014	493	2999	10.65	3.93	3.82	27.57
2010 09	2.39	0.76	...	...	...	...	2.81	0.028	129	5802	3.37	2.02	1.95	6.98
2010 10	2.29	0.66	...	...	...	...	3.66	0.011	8	1235	1.70	1.34	0.88	3.18
2010 11	2.18	0.10	...	...	...	...	0.37	0.097	29	849	4.69	2.91	1.15	10.91
2010 12	2.29	0.39	...	...	...	...	4.80	0.006	56	394	5.22	2.97	1.56	12.73
2011 01	2.13	0.17	...	...	...	...	2.27	0.030	81	661	5.50	3.02	1.68	13.53
Average	2.29 ± 0.09	0.60 ± 0.32	1.3	0.02	14.56 ± 7.60	2.76 ± 1.36	2.18 ± 1.62	0.057 ± 0.061	4948 ± 2245	55	5.42	3.00	2.30	12.54
Model: Pascucci free tilt														
2009 11	2.30	0.62	1.102	0.16	8.93	1.74	1.55	0.025	6018	349	4.65	4.37	2.52	7.25
2009 12	2.27	1.00	1.148	0.15	19.96	3.73	0.10	0.120	6417	164	9.14	3.65	3.29	25.22
2010 02	2.43	0.95	1.088	2.72	...	...	1.10	0.176	46	347	3.06	2.37	2.63	4.52
2010 08	2.33	0.78	2.330	0.70	...	...	4.75	0.005	1298	1208	16.17	7.69	7.96	37.09
2010 09	2.39	0.78	1.153	0.51	...	...	2.70	0.027	422	6353	2.92	1.71	1.67	6.11
2010 10	2.32	0.71	0.353	0.29	...	...	4.92	0.003	13	1256	4.43	2.11	1.19	12.06
2010 11	2.24	0.29	6.879	0.95	...	...	0.24	0.000	691	1511	5.22	2.93	1.37	12.52
2010 12	2.23	0.38	2.324	0.96	...	...	4.97	0.000	330	780	114.24	22.38	14.86	370.25
2011 01	2.20	0.23	1.108	0.87	...	...	2.08	0.037	1391	1971	1.62	1.25	0.87	3.01
Average	2.30 ± 0.08	0.64 ± 0.28	1.943 ± 1.955[b]	0.51 ± 1.03	14.45 ± 7.80	2.73 ± 1.40	2.49 ± 1.97	0.044 ± 0.062	4223 ± 1319	522	17.94	5.39	4.04	53.12

Notes.
[a] The variations either assume the disk has zero tilt, a fixed tilt, or a per epoch tilt with respect to the orbital plane. The averaged inclination of 1°.33 ± 0°.67 agrees well with the multi epoch minimizations. The variations in scale height appear to be real.
[b] Excluding the 2010 11 result, this becomes 1.33 ± 0.67 in agreement with our fixed tilt model.

A.7. 2011-09-18 and Later

All of the post-eclipse images are displayed in Figure A52. Much like the ingress phase images, these reconstructions show that the F-star has no egregious asymmetries that cannot be explained by UV coverage or reconstruction artifacts. We note that two of the post-eclipse epochs (2011-10-10 and 2011-11-03) do show non-zero closure phase and different locations of the first visibility null, indicating that the F-star may harbor spots or be slightly oblate. Both of these effects, if real, are insignificant compared to the variations that the disk imparts upon the interferometric data during the eclipse. We will
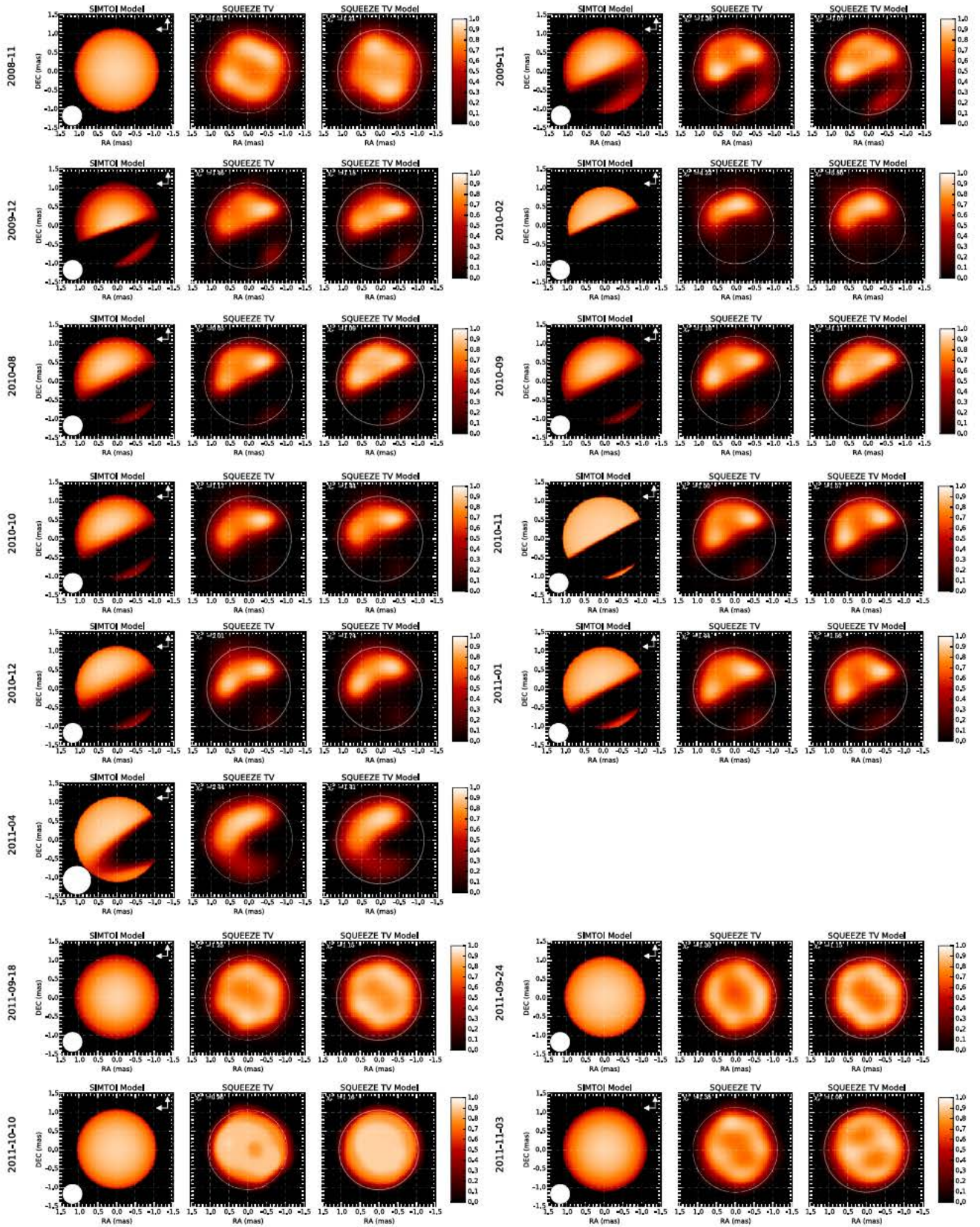
Figure 5. Best fit models and SQUEEZE total variation (TV) regularizer reconstructions for each CHARA epoch. All images are displayed with North up and east to the left. The 0.5 mas resolution limit of MIRC and 0.7 mas limit of CLIMB are indicated by the solid white circles in the lower left of the first image. The remaining white circle indicates the best fit SIMTOI angular diameter. In each epoch the columns contain the following images (left) the best fit model from SIMTOI, (center) the model independent reconstruction of the interferometric data, and (right) a reconstruction of synthetic data generated from the model as described in Section 4. For a detailed discussion of each epoch please see the Appendix.

(The complete figure set (7 images) is available.)

attempt to quantify the presence of spots or asymmetry in greater detail in a future publication.

APPENDIX B
CREATION OF THE SILHOUETTE IMAGE

The silhouette image is created by aligning and combining the individual SQUEEZE images. Because SQUEEZE images are flux centered and frequently contain stray flux, the image was generated manually using the following process. SIMTOI was used to generate a series of 768×768 pixel images consisting of a uniform disk F-star aligned according to the orbital elements specified in this work. These images, along with the original SQUEEZE reconstructions, were imported into GIMP (a popular image editing program) as layers. During the import process, each FITS image was converted to 256 levels of gray. Individual SQUEEZE layers were aligned with the corresponding SIMTOI prediction with the aid of a ranged color selection tool used to highlight the average background plus 6%. The layers were combined using the "screen" layer mode which computes the output value, C, from overlays A and B according to the following equation:

$$C = 255 - [(255 - A) \cdot (255 - B)]/255.$$

Because each image is of unit flux, this scaling approach preserves the appearance of the original images. After this, a black mask was created that decreased the appearance of stray flux in the individual images. This last step was subjective and therefore used sparingly. Finally, the image was gamma-corrected $\gamma = -1.5$ in order to make the appearance of the southern limb of the F-star more obvious to the reader.

REFERENCES

Andrews, S. M., Wilner, D. J., Hughes, A. M., Qi, C., & Dullemond, C. P. 2009, ApJ, 700, 1502
Armstrong, J. T., Mozurkewich, D., Rickard, L. J., et al. 1998, ApJ, 496, 550
Backman, D. E., Becklin, E. E., Cruikshank, D. P., et al. 1984, ApJ, 284, 799
Baron, F., & Kloppenborg, B. 2010, in Optical and Infrared Interferometry II, Vol. 7734, ed. W. C. Danchi, F. Delplancke & J. K. Rajagopal (San Diego, CA: SPIE), 77344D
Baron, F., Monnier, J. D., & Kloppenborg, B. 2010, in Optical and Infrared Interferometry II, Vol. 7734, ed. W. C. Danchi, F. Delplancke & J. K. Rajagopal (San Diego, CA: SPIE), 77342I
Baron, F., & Young, J. S. 2008, Proc. SPIE, 7013, 70133X
Benson, J. A., Hummel, C. A., & Mozurkewich, D. 2003, Proc. SPIE, 4838, 358
Budaj, J. 2011, A&A, 532, L12
Buscher, D. F. 1994, in Proc. 158th IAU Symp., Very High Angular Resolution Imaging, ed. J. G. Robertson & W. J. Tango (Dordrecht: Kluwer), 91
Carroll, S. M., Guinan, E. F., McCook, G. P., & Donahue, R. A. 1991, ApJ, 367, 278
Chadima, P., Harmanec, P., Yang, S., et al. 2010, IBVS, 5937, 1
Che, X., Monnier, J. D., & Webster, S. 2010, Proc. SPIE, 7734, 77342V
Claret, A. 2000, A&A, 363, 1081
Claret, A., & Hauschildt, P. H. 2003, A&A, 412, 241
Colavita, M. M., Wallace, J. K., Hines, B. E., et al. 1999, ApJ, 510, 505
Ferluga, S. 1989, MmSAI, 60, 211
Ferluga, S. 1990, A&A, 238, 270
Feroz, F., & Hobson, M. P. 2008, MNRAS, 384, 449
Feroz, F., Hobson, M. P., & Bridges, M. 2009, MNRAS, 398, 1601
Feroz, F., Hobson, M. P., Cameron, E., & Pettitt, A. N. 2013, arXiv:1306.2144
Fields, D. L., Albrow, M. D., An, J., et al. 2003, ApJ, 596, 1305
Fritsch, J. M. 1824, in Astronomisches Jahrbuch, 252

Griffin, R. E., & Stencel, R. E. 2013, PASP, 125, 775
Guinan, E. F., Dewarf, L. E., Guinan, E. F., & DeWarf, L. E. 2002, in IAU Colloquium 187, Exotic Stars as Challenges to Evolution, 279, ed. C. A. Tout & W. Van Hamme (San Francisco, CA: ASP), 121
Guinan, E. F., Mayer, P., Harmanec, P., et al. 2012, A&A, 546, A123
Heintz, W. D., & Cantor, B. A. 1994, PASP, 106, 363
Hestroffer, D. 1997, A&A, 327, 199
Hoard, D. W., Howell, S. B., & Stencel, R. E. 2010, ApJ, 714, 549
Hoard, D. W., Ladjal, D., Stencel, R., & Howell, S. 2012, ApJL, 748, L28
Hopkins, J. L. 2012, JAVSO, 40, 633
Huang, S. S. 1965, ApJ, 141, 976
Huang, S. S. 1974, ApJ, 189, 485
Hummel, C. A., Benson, J. A., Hutter, D. J., et al. 2003, AJ, 125, 2630
Ireland, M. J. 2006, Proc. SPIE, 6268, 62681T
Kemp, J. C., Henson, G. D., Kraus, D. J., et al. 1986, ApJL, 300, L11
Kloppenborg, B., & Baron, F. 2012a, LibOI: The OpenCL Interferometry Library, https://github.com/bkloppenborg/liboi
Kloppenborg, B., & Baron, F. 2012b, SIMTOI: SImulation and Modeling Tool for Optical Interferometry, https://github.com/bkloppenborg/simtoi
Kloppenborg, B., Stencel, R., Monnier, J. D., et al. 2010, Natur, 464, 870
Kloppenborg, B. K. 2012, PhD thesis, Univ. Denver
Kloppenborg, B. K., Hopkins, J. L., & Stencel, R. E. 2012, JAVSO, 40, 647
Kopal, Z. 1954, Obs, 74, 14
Kumar, S. 1987, MNRAS, 225, 823
Lafrasse, S., Mella, G., Bonneau, D., et al. 2010, Proc. SPIE, 7734, 77344E
Lambert, D. L., & Sawyer, S. R. 1986, PASP, 98, 389
Leadbeater, R., Buil, C., Garrel, T., et al. 2012, JAVSO, 40, 729
Lissauer, J. J., Wolk, S. J., Griffith, C. A., & Backman, D. E. 1996, ApJ, 465, 371
Lourakis, M. I. A. 2005, levmar: Levenberg Marquardt nonlinear least squares algorithms in C/C++, http://www.ics.forth.gr~lourakis/levmar/
Ludendorff, H. 1903, AN, 164, 81
Maestro, V., Che, X., Huber, D., et al. 2013, MNRAS, 434, 1321
Marshall, P., Pedretti, E., & Thureau, N. 2006, Proc. SPIE, 6268, 62681P
Monnier, J. D., Pedretti, E., & Thureau, N. 2006, Proc. SPIE, 6268, 62681P
Monnier, J. D., Berger, J. P., Millan Gabet, R., & ten Brummelaar, T. A. 2004, Proc. SPIE, 5491, 1370
Monnier, J. D., Anderson, M., Baron, F., et al. 2010, Proc. SPIE, 7734, 77340G
Monnier, J. D., Zhao, M., Pedretti, E., et al. 2007, Sci, 317, 342
Mourard, D., Harmanec, P., Stencel, R., et al. 2012, A&A, 544, A91
Mozurkewich, D., Armstrong, J. T., Hindsley, R. B., et al. 2003, AJ, 126, 2502
Muthumariappan, C., & Parthasarathy, M. 2012, MNRAS, 423, 27
Nordgren, T. E., Sudol, J. J., & Mozurkewich, D. 2001, AJ, 122, 2707
Pascucci, I., Wolf, S., Steinacker, J., et al. 2004, A&A, 417, 793
Pauls, T. A., Young, J. S., Cotton, W. D., & Monnier, J. D. 2005, PASP, 117, 1255
Perryman, M. A. C., Lindegren, L., & Kovalevsky, J. 1997, A&A, 323, L49
Ricci, L., Robberto, M., & Soderblom, D. R. 2008, AJ, 136, 2136
Russell, H. N. 1912a, ApJ, 35, 315
Russell, H. N. 1912b, ApJ, 35, 315
Sadakane, D., Kambe, E., Satō, B., Honda, S., & Hashimoto, O. 2010, PASJ, 62, 1381
Saitō, M., & Kitamura, M. 1986, Ap&SS, 122, 387
Shapley, H. 1915, CoPri, 3
Stefanik, R. P., Torres, G., Lovegrove, J., et al. 2010, AJ, 139, 1254
Stencel, R. E., Creech Eakman, M., Hart, A., et al. 2008, ApJL, 689, L137
Stencel, R. E., Kloppenborg, B. K., Wall, R. E., et al. 2011, AJ, 142, 174
Strand, K. A. 1959, AJ, 64, 346
Sturmann, J., ten Brummelaar, T., Sturmann, L., & McAlister, H. A. 2010, Proc. SPIE, 7734, 77343A
Takeuti, M. 1986, Ap&SS, 121, 127
Takeuti, M. 2011, PASJ, 63, 323
Tallon Bosc, I., Tallon, M., Thiebaut, E., et al. 2008, Proc. SPIE, 7013, 70131J
ten Brummelaar, T. A., McAlister, H. A., Ridgway, S. T., et al. 2005, ApJ, 628, 453
ten Brummelaar, T. A., Sturmann, J., McAlister, H. A., et al. 2012, Proc. SPIE, 8445, 84453C
van de Kamp, P. 1978, AJ, 83, 975
van Leeuwen, F. 2007, A&A, 474, 653
van Leeuwen, F. 2008, yCat: I/311
Wilson, R. E. 1971, ApJ, 170, 529